Cronfa - Swansea University Open Access Repository

_____

This is an author produced version of a paper published in:
International Journal for Numerical Methods in Engineering

_____

Cronfa URL for this paper:
http://cronfa.swan.ac.uk/Record/cronfa29689

_____

Paper:

Bagwell, S., Ledger, P., Gil, A., Mallett, M. & Kruip, M. (2017). A linearised hp-finite element framework for Acousto-Magneto-Mechanical coupling in axisymmetric MRI scanners. *International Journal for Numerical Methods in Engineering*
http://dx.doi.org/10.1002/nme.5559

_____

http://www.swansea.ac.uk/iss/researchsupport/cronfa-support/

A linearised $hp-$finite element framework for acousto-magneto-mechanical coupling in axisymmetric MRI scanners

Scott Bagwell[1], Paul D Ledger[1*,†] (iD), Antonio J Gil[1], Mike Mallett[2] and Marcel Kruip[2]

[1]*Zienkiewicz Centre for Computational Engineering, College of Engineering, Swansea University, Bay Campus, Swansea, SA1 8EN, UK*
[2]*Siemens PLC, Healthcare Sector, MR Magnet Technology, Wharf Road, Eynsham, Witney, OX29 4BP, Oxon, UK*

SUMMARY

We propose a new computational framework for the treatment of acousto-magneto-mechanical coupling that arises in low-frequency electro-magneto-mechanical systems such as magnetic resonance imaging scanners. Our transient Newton−Raphson strategy involves the solution of a monolithic system obtained from the linearisation of the coupled system of equations. Moreover, this framework, in the case of excitation from static and harmonic current sources, allows us to propose a simple linearised system and rigorously motivate a single-step strategy for understanding the response of systems under different frequencies of excitation. Motivated by the need to solve industrial problems rapidly, we restrict ourselves to solving problems consisting of axisymmetric geometries and current sources. Our treatment also discusses in detail the computational requirements for the solution of these coupled problems on unbounded domains and the accurate discretisation of the fields using $hp-$finite elements. We include a set of academic and industrially relevant examples to benchmark and illustrate our approach. Copyright © 2017 The Authors. *International Journal for Numerical Methods in Engineering* Published by John Wiley & Sons, Ltd.

1. INTRODUCTION

Magnetic resonance imaging (MRI) has become a widely used and popular tool in the medical industry capable of diagnosis of many medical ailments, such as tumours, damaged cartilage and internal bleeding as well as its use in neuroimaging. The most popular type of magnet used in these devices are superconducting magnets, consisting of conducting wire contained within a supercooled vessel of liquid helium known as the cryostat, which achieve the field strengths required for high-resolution imaging. Figure 1 shows a typical setup of an MRI scanner, consisting essentially of four main components: the main magnet coils, secondary magnetic coils, the cryostat (comprised of a set of radiation shields that encapsulate the liquid helium immersed magnetic coils) and resistive gradient coils. A set of main magnetic coils produce a strong uniform stationary magnetic field across the radial section of the scanner, required to align the protons of the hydrogen atoms in the patient in the axial direction. The secondary magnetic coils are used to minimise the large stray magnetic fields arising outside of the scanner. The cryostat consists of a set of metallic vessels in vacuum to maintain the supercooled magnet temperatures and shield the coils from radiation. A set of resistive coils inside the imaging volume, known as gradient coils, produce pulsed magnetic field gradients that excite certain regions of the protons to generate an image of the patient.

---

*Correspondence to: Paul Ledger, Zienkiewicz Centre for Computational Engineering, College of Engineering, Swansea University, Bay Campus, Swansea SA1 8EN, UK.
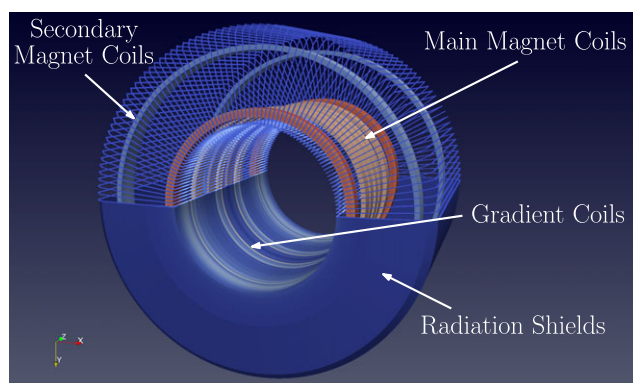†E-mail: p.d.ledger@swansea.ac.uk

---

Figure 1. Primary components of a simplified clinical magnetic resonance imaging scanner.

Recent developments in MRI scanner design have increased the field strength of the main magnet, improved the transient gradient coil current signature and considered changes in bore geometry in order to improve the quality of MRI images. However, this also introduces new challenges because image quality must also be balanced with the needs of clinical efficiency and patient safety [1]. Transient magnetic fields produce eddy currents in conducting components, which, in turn, perturb the magnetic field and generate Lorentz forces, exerting electro-mechanical stresses causing them to vibrate and deform [2]. The vibrations also cause perturbations of the surrounding air, which produce an acoustic pressure field. These phenomena can have undesired effects causing imaging artefacts (ghosting), decreased component life and uncomfortable conditions for the patient, because of the noise from mechanical vibrations. Minimising ghosting effects, keeping noise levels to acceptable limits and ensuring patient safety are key criteria for new MRI scanner designs.

The consistent exposure to time-varying magnetic fields during a scan procedure has resulted in patients experiencing 'tingling' sensations [3]. During some scans, when patients have been exposed to high sound levels, adverse effects have also been reported [4,5]. Current guidelines [1] state 'there is little risk of a permanent threshold shift in hearing in those exposed to noise associated with MRI procedures on a one-off or occasional basis'. It goes on to say that, in current low-frequency MRI scanners, clinically significant effects on hearing are unlikely in most subjects for noise levels below 85 dB(A) of scans lasting less than an hour. Nevertheless, 'IEC recommend that hearing protection should be used if equipment is capable of producing more than 99 dB(A)'. Many attempts have been made to measure the sound profiles of these harmful noise levels [6,7] as well as proposing methods to reduce them, such as active noise-cancelling technologies [8].

Experimental prototyping and testing of new scanner designs is expensive, and to reduce this cost, there is considerable interest in the development of accurate computational tools, which can aid the design process. However, the development of such tools is challenging due to complexity that results from the coupled physics of electromagnetism, mechanics and acoustics and the non-trivial task of accurately modelling the complex field behaviour.

Previously, there has been interest in applying commercial multi-physics finite element (method) (FE(M)) packages, such as COMSOL [9], Ansys [10] and NACS [11], to simulate the coupled nature of MRI scanners. Rausch et al. have presented an approach based on the FEM-BEM (boundary element method) program CAPA [12] for the magneto-mechanical coupling effects of an MRI scanner using a low-order discretisation [13]. This important three-dimensional simulation was extended to include acoustic effects in [14] and, to the best of the authors' knowledge, is the only fully coupled simulation of a complete MRI scanner that has been presented to date. To describe the electromagnetic forces, they adopt the approach of Kaltenbacher, which employs a layer of elements adjacent to the conductor for their computation [15]. In our previous work [2,16–18], we advocated an alternative approach, which allows us to avoid the direct computation of electromotive forces and instead work entirely with a physically motivated Maxwell stress tensor. Others have attempted to model these complex physical effects to aid the design of the MRI magnetic coils [19,20], to analyse the plane strain effects on superconducting solenoids [21] and the effects of the magnetic field exposure on the patient [22].

The simulation of MRI scanners also builds on the expanding literature devoted to magneto-mechanics and coupled problems including FEM-BEM coupling [23,24], magneto-mechanical damping machines [25], magneto-mechanical effects on material parameters [26], enhanced basis functions for magneto-mechanical coupling [27] and strongly coupled systems [28]. When the coupling includes acoustic effects, careful treatment of the far field boundary is also required and techniques such as perfectly matched layers (PML), FEM-BEM coupling, infinite elements and absorbing boundary conditions have been developed for this (see, e.g. [29] for a recent review).

Although commercial codes provide an efficient environment for many problems, our interest lies in providing a low-cost dedicated industrial design tool. This tool should operate over a wide range of frequencies more effectively in order to predict the response from an analysis of general gradient coil time signatures, which can be decomposed by Fourier expansion. As such, not only do we require a reliable means of treating the coupled nature of acousto-magneto-mechanical problems, but we also need to be able to accurately resolve the potentially small skin depth in conducting components as well as accurately resolve the propagation of acoustic waves. The aforementioned commercial codes are typically designed with low-order FE discretisations in mind, which require dense meshes for handling the small skin depths and wave propagation at higher frequencies. On the other hand, $hp-$FE discretisations offer possibilities for high accuracy on locally refined meshes and have been shown to accurately resolve the skin depth in the conducting components [30], handle the complex coupling [16−18] and to resolve the propagation of the acoustic waves [31] and we, therefore, choose to adopt them here. Furthermore, in the computation of unbounded domains using a PML, they have also been shown to offer superior performance [32].

Building on the established $hp-$FEM methodology, the main novelty of our work is to provide a new rigorous theoretical framework for the simulation of acousto-magneto-mechanical effects in MRI scanners, which forms the basis of our design tool. We undertake the consistent linearisation of the transient equations and arrive at a simplified monolithic single-step strategy in the case of harmonic gradient coil excitations. It greatly improves on our previous work [2], which required non-physically motivated simplifying assumptions and resulted in a fixed point strategy with a growth of iterations for increasing frequency. We also extend our framework to incorporate the effects of the acoustic field and propose a rigorous set of interface conditions, which couple the various physics together. The entire framework is suitable for three-dimensional geometries discretised by $hp-$FEM, but such simulations would be prohibitively expensive for the industrial design cycle. As our interest lies in the development of a rapid design tool, we focus on the simulation of problems on axisymmetric geometries.

The presentation of the material proceeds as follows: In Section 2, we outline the governing equations, the coupling between the fields and present a fully coupled non-linear transient transmission problem. Section 3 presents the consistent linearisation of the weak form of the transmission problem, and we derive a simplified monolithic strategy in the case of harmonic gradient coil excitations. Then, in Section 4, we briefly discuss the reduction to axisymmetric geometry, the computational far field treatment and the $hp-$FE discretisation. Section 5 presents a selection of numerical case studies to validate each physical field independently and highlights the computational challenges of small skin depth and high-frequency wave propagation. Then we present a series of results for complex coupled case studies of industrial relevance before closing with concluding remarks.

2. COUPLING APPROACH

In the following, we describe the governing equations and coupling methodologies that link the electromagnetic, mechanical and acoustic behaviour of an MRI scanner. We begin, in Section 2.1, with the transient eddy current model to describe the electromagnetic response from a conducting region Ω_c when illuminated by a low-frequency background magnetic field. This field arises from a current source $\boldsymbol{J}^s$ with support in an unbounded region of free space $\mathbb{R}^3 \backslash \Omega_c$, as illustrated in Figure 2. Then, in Section 2.2, we present the corresponding transient mechanical response of Ω_c resulting from electromagnetic stresses generated in this region. Finally, in Section 2.3, we present the transient
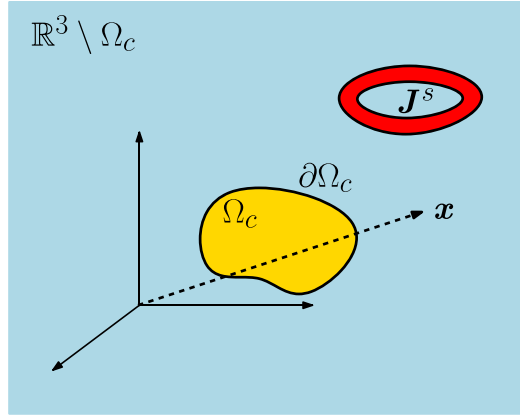
Figure 2. Conducting region Ω_c excited by coils contained within the unbounded $\mathbb{R}^3 \backslash \Omega_c$ space.

acoustic response resulting from the vibration of Ω_c in $\mathbb{R}^3 \backslash \Omega_c$. The complete coupled transmission problem is stated in 2.4.

2.1. Electromagnetic description

For our chosen application, the transient eddy current approximation of Maxwell's equations is valid [2], where the displacement current terms are neglected because of the high conductivity of the conducting components and the low frequency of the exciting currents. A rigorous justification involves the topology of the conducting region [33]. Defining E, H, D, B as the electric, magnetic, electric flux and magnetic flux intensity vectors, respectively, and introducing a vector potential A such that $B = \nabla \times A$, this model can be described by[‡]

$$\nabla \times (\mu^{-1} \nabla \times A) = J^s + J^o + J^l = J^s - \gamma \frac{\partial A}{\partial t} + \gamma \frac{\partial u}{\partial t} \times (\nabla \times A) \qquad \text{in } \mathbb{R}^3, \tag{1a}$$

$$\nabla \cdot A = 0 \qquad \text{in } \mathbb{R}^3 \backslash \Omega_c, \tag{1b}$$

$$A = O\left(|x|^{-1}\right) \qquad \text{as } |x| \to \infty, \tag{1c}$$

where we assume x to be measured from the centre of Ω_c. The previous equation assumes the regions to be homogenous and isotropic, such that $B = \mu H$ and $J^o = \gamma E$ where γ denotes the electrical conductivity and μ the magnetic permeability. The solenoidal external current sources J^s are assumed to lie in free space, $\mathbb{R}^3 \backslash \Omega_c$, where $\gamma = 0$ and $\mu = \mu_0 = 4\pi \times 10^{-7}$H/m. The term $J^l = \gamma \partial u / \partial t \times \nabla \times A$ denotes the Lorentz currents where u is the mechanical displacement in the conducting region Ω_c.

The vector potential A satisfies the transmission conditions on the conductor boundary $\partial \Omega_c$

$$n \times [A]_{\partial \Omega_c} = \mathbf{0}, \qquad n \times [\mu^{-1} \nabla \times A]_{\partial \Omega_c} = \mathbf{0},$$

where $[\cdot]_{\partial \Omega_c}$ denotes the jump on this interface and n is a unit outward normal vector to $\partial \Omega_c$.

2.2. Mechanical description

The conducting region Ω_c is assumed to behave elastically and the mechanical displacements u to satisfy

$$\nabla \cdot (\sigma^m(u) + \sigma^e(A)) = \rho \frac{\partial^2 u}{\partial t^2} \qquad \text{in } \Omega_c, \tag{2}$$

[‡]The temporal gauge has been applied in Ω_c and the Coulomb gauge in $\mathbb{R}^3 \backslash \Omega_c$ [30]. Note we set $A = O\left(|x|^{-1}\right)$ as $x \to \infty$ according to the mathematical model described by Ammari, Buffa and Nédélec; [33] here, the big O notation implies that the rate is at least as fast as $|x|^{-1}$ and can be faster in practice; for details, see the aforementioned paper.

where

$$\boldsymbol{\sigma}^m(\boldsymbol{u}) := \lambda \mathrm{tr}(\boldsymbol{\varepsilon}(\boldsymbol{u}))\boldsymbol{I} + 2G\boldsymbol{\varepsilon}(\boldsymbol{u}),$$

is the mechanical contribution to the Cauchy stress tensor, λ, G denote the Lamé parameters, $\boldsymbol{\varepsilon} := \left(\nabla \boldsymbol{u} + \nabla \boldsymbol{u}^T\right)/2$ the linear strain tensor, $\boldsymbol{I}$ the identity tensor, ^{T} the transpose and

$$\begin{aligned}
\boldsymbol{\sigma}^e(A) &:= \mu\left(\boldsymbol{H} \otimes \boldsymbol{H} - \frac{1}{2}|\boldsymbol{H}|^2\boldsymbol{I}\right) \\
&= \mu^{-1}\left(\nabla \times \boldsymbol{A} \otimes \nabla \times \boldsymbol{A} - \frac{1}{2}|\nabla \times \boldsymbol{A}|^2\boldsymbol{I}\right),
\end{aligned}$$

is the magnetic component of the Maxwell stress tensor [2]. In Equation (2), we have already used the fact that the magneto-ponderomotive forcing term can be expressed as $\boldsymbol{f}^e = \nabla \cdot \boldsymbol{\sigma}^e$. We write $\partial\Omega_c = \partial\Omega_c^D \cup \partial\Omega_c^N$ and fix $\boldsymbol{u} = \boldsymbol{u}^D$ on $\partial\Omega_c^D$ in order to stop the conducting component floating away.

2.3. Pressure description

In free space, $\boldsymbol{\sigma}^m$ has only a volumetric part $\boldsymbol{\sigma}^m_{vol} := \hat{p}\boldsymbol{I} = \kappa(\nabla \cdot \boldsymbol{u})\boldsymbol{I}$ where $\hat{p}$ is some pressure field. This means that (2) reduces to the scalar wave equation with a sourcing term

$$\nabla^2\hat{p} - \frac{1}{c^2}\frac{\partial^2\hat{p}}{\partial t^2} = -\nabla \cdot (\nabla \cdot \boldsymbol{\sigma}^e) \qquad \text{in } \mathbb{R}^3\backslash\Omega_c, \tag{3}$$

where $c := \sqrt{\kappa/\rho}$ is the speed of sound and κ denotes the bulk modulus of the medium. This must be accompanied by the associated radiation condition

$$\lim_{|\boldsymbol{x}|\to\infty}\left(\frac{\partial\hat{p}}{\partial|\boldsymbol{x}|} + \frac{\partial\hat{p}}{\partial t}\right) = O(|\boldsymbol{x}|^{-1}). \tag{4}$$

The source term in (3) is only non-zero in the support of $\boldsymbol{J}^s$[§]; this can be seen by considering the alternative form of $\boldsymbol{f}^e$ in free space below[¶]

$$\boldsymbol{f}^e = \nabla \cdot \boldsymbol{\sigma}^e = -\mu_0\,\boldsymbol{H} \times \nabla \times \boldsymbol{H} = -\nabla \times \boldsymbol{A} \times \boldsymbol{J}^s = -\nabla \times \boldsymbol{A} \times (\nabla \times \mu_0^{-1}\nabla \times \boldsymbol{A}), \tag{5}$$

and thus it follows that in the same region

$$\nabla \cdot \boldsymbol{f}^e = \nabla \cdot (\nabla \cdot \boldsymbol{\sigma}^e) = \mu_0(\boldsymbol{H} \cdot \nabla \times \boldsymbol{J}^s - |\boldsymbol{J}^s|^2). \tag{6}$$

Taking this into account, on the interface $\partial\Omega_c$ shown in Figure 3, the pressure field, mechanical displacements and stresses are coupled by the transmission conditions

$$\begin{aligned}
(\boldsymbol{\sigma}^m + \boldsymbol{\sigma}^e)|^-_{\partial\Omega_c}\,\boldsymbol{n} &= (\hat{p}\boldsymbol{I} + \boldsymbol{\sigma}^e)|^+_{\partial\Omega_c}\,\boldsymbol{n}, \\
\rho^+\left.\frac{\partial^2\boldsymbol{u}}{\partial t^2}\right|^-_{\partial\Omega_c} \cdot \boldsymbol{n} &= (\nabla\hat{p} + \nabla \cdot \boldsymbol{\sigma}^e)|^+_{\partial\Omega_c} \cdot \boldsymbol{n},
\end{aligned}$$

Note that the latter condition also further reduces to

$$\nabla\hat{p}|^+_{\partial\Omega_c^D} \cdot \boldsymbol{n} = 0, \qquad \rho^+\left.\frac{\partial^2\boldsymbol{u}}{\partial t^2}\right|^-_{\partial\Omega_c^N} \cdot \boldsymbol{n} = (\nabla\hat{p} + \nabla \cdot \boldsymbol{\sigma}^e)|^+_{\partial\Omega_c} \cdot \boldsymbol{n},$$

in light of the known Dirichlet displacement condition on $\partial\Omega_c^D$ for the mechanical problem.

[§]Here, we assume Biot–Savart coils. If the coils are instead treated as rigid or deformable conducting bodies, then their support instead forms part of Ω_c

[¶]We recall here the relationship between the curl and gradient operators $(\nabla\boldsymbol{H})\boldsymbol{H} - 1/2\nabla(\boldsymbol{H} \cdot \boldsymbol{H}) = -\boldsymbol{H} \times (\nabla \times \boldsymbol{H})$.
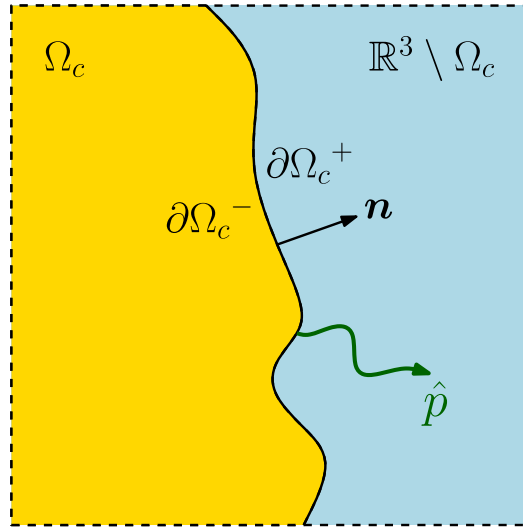
Figure 3. Interface conditions at the conductor boundary.

2.4. Coupled transmission problem

Combining the statements from the previous Sections 2.1, 2.2 and 2.3, we arrive at the following transmission problem for describing our coupled acousto-magneto-mechanical system in a time period $[0, T]$: Find $(A, u, \hat{p})(t) \in (\mathbb{R}^3 \times \mathbb{R}^3 \times \mathbb{R})[0, T]$ such that

$$\nabla \times (\mu^{-1} \nabla \times A) + \gamma \frac{\partial A}{\partial t} = J^s + \gamma \frac{\partial u}{\partial t} \times (\nabla \times A) \qquad \text{in } \mathbb{R}^3, \tag{7a}$$

$$\nabla \cdot A = 0 \qquad \text{in } \mathbb{R}^3 \backslash \Omega_c, \tag{7b}$$

$$\nabla \cdot (\sigma^m(u) + \sigma^e(A)) = \rho \frac{\partial^2 u}{\partial t^2} \qquad \text{in } \Omega_c, \tag{7c}$$

$$\nabla^2 \hat{p} - \frac{1}{c^2} \frac{\partial^2 \hat{p}}{\partial t^2} = -\nabla \cdot (\nabla \cdot \sigma^e(A)) \qquad \text{in } \mathbb{R}^3 \backslash \Omega_c, \tag{7d}$$

$$A = O\left(|x|^{-1}\right), \tag{7e}$$

$$\lim_{|x| \to \infty} \left(\frac{\partial \hat{p}}{\partial |x|} + \frac{\partial \hat{p}}{\partial t} \right) = O(|x|^{-1}) \qquad \text{as } |x| \to \infty, \tag{7f}$$

$$u = u^D, \tag{7g}$$

$$\nabla \hat{p}|^+_{\partial \Omega_c^D} \cdot n = 0 \qquad \text{on } \partial \Omega_c^D, \tag{7h}$$

$$\rho^+ \frac{\partial^2 u}{\partial t^2} \bigg|^-_{\partial \Omega_c^N} \cdot n = (\nabla \hat{p} + \nabla \cdot \sigma^e(A))|^+_{\partial \Omega_c} \cdot n \qquad \text{on } \partial \Omega_c^N, \tag{7i}$$

$$n \times [A]_{\partial \Omega_c} = 0, \tag{7j}$$

$$n \times [\mu^{-1} \nabla \times A]_{\partial \Omega_c} = 0, \tag{7k}$$

$$(\sigma^e(A) + \sigma^m(u))|^-_{\partial \Omega_c} n = (\hat{p}I + \sigma^e(A))|^+_{\partial \Omega_c} n \qquad \text{on } \partial \Omega_c, \tag{7l}$$

$$A(t = 0) = 0 \qquad \text{in } \mathbb{R}^3, \tag{7m}$$

$$u(t = 0) = \frac{\partial u}{\partial t}(t = 0) = 0 \qquad \text{in } \Omega_c, \tag{7n}$$

$$\hat{p}(t = 0) = \frac{\partial \hat{p}}{\partial t}(t = 0) = 0 \qquad \text{in } \mathbb{R}^3 \backslash \Omega_c, \tag{7o}$$

where we have chosen to set the initial conditions for the fields to be zero, corresponding to a system at rest at $t = 0$. An illustration of the fully coupled system is shown in Figure 4.
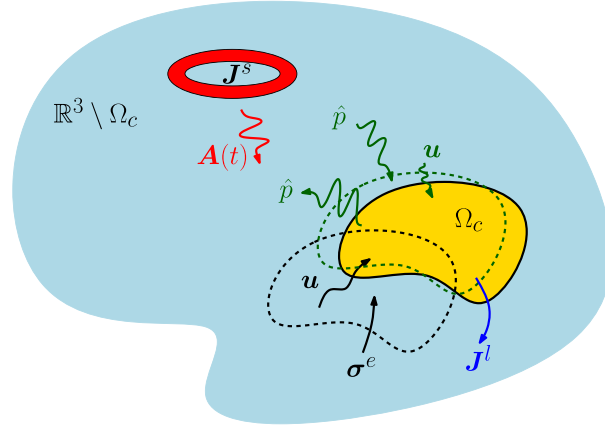
Figure 4. Physical representation of the coupling effects in an magnetic resonance imaging environment.

For our desired application, the system (7) is excited through the current source $\boldsymbol{J}^s(t)$. In practice, the application allows for the decomposition $\boldsymbol{J}^s(t) = \boldsymbol{J}^{DC} + \boldsymbol{J}^{AC}(t)$, where $\boldsymbol{J}^{DC}$ corresponds to the static current source of the main magnetic coils and $\boldsymbol{J}^{AC}(t)$ the transient current source of the gradient coils [2]. This decomposition, illustrated in Figure 5, allows us to introduce the following static problem: find $\boldsymbol{A}^{DC}, \boldsymbol{u}^{DC}, \hat{p}^{DC} \in \mathbb{R}^3 \times \mathbb{R}^3 \times \mathbb{R}$ such that

$$\nabla \times (\mu^{-1}\nabla \times \boldsymbol{A}^{DC}) = \boldsymbol{J}^{DC} \qquad\qquad \text{in } \mathbb{R}^3, \tag{8a}$$

$$\nabla \cdot \boldsymbol{A}^{DC} = 0 \qquad\qquad \text{in } \mathbb{R}^3, \tag{8b}$$

$$\nabla \cdot (\boldsymbol{\sigma}^m(\boldsymbol{u}^{DC}) + \boldsymbol{\sigma}^e(\boldsymbol{A}^{DC})) = 0 \qquad\qquad \text{in } \Omega_c, \tag{8c}$$

$$\nabla^2 \hat{p}^{DC} = -\nabla \cdot (\nabla \cdot \boldsymbol{\sigma}^e(\boldsymbol{A}^{DC})) \qquad\qquad \text{in } \mathbb{R}^3\backslash\Omega_c, \tag{8d}$$

$$\boldsymbol{A}^{DC} = O\left(|\boldsymbol{x}|^{-1}\right), \tag{8e}$$

$$\hat{p}^{DC} = O(|\boldsymbol{x}|^{-1}) \qquad\qquad \text{as } |\boldsymbol{x}| \to \infty, \tag{8f}$$

$$\boldsymbol{u}^{DC} = \boldsymbol{u}^D_{DC} \qquad\qquad \text{on } \partial\Omega_c^D, \tag{8g}$$

$$\boldsymbol{n} \times [\boldsymbol{A}^{DC}]_{\partial\Omega_c} = \boldsymbol{0}, \tag{8h}$$

$$\boldsymbol{n} \times [\mu^{-1}\nabla \times \boldsymbol{A}^{DC}]_{\partial\Omega_c} = \boldsymbol{0}, \tag{8i}$$

$$\left(\nabla\hat{p}^{DC} + \nabla \cdot \boldsymbol{\sigma}^e(\boldsymbol{A}^{DC})\right)\Big|_{\partial\Omega_c}^+ \cdot \boldsymbol{n} = 0, \tag{8j}$$

$$\left(\boldsymbol{\sigma}^m(\boldsymbol{u}^{DC}) + \boldsymbol{\sigma}^e(\boldsymbol{A}^{DC})\right)\Big|_{\partial\Omega_c}^- \boldsymbol{n} = \left(\hat{p}^{DC}\boldsymbol{I} + \boldsymbol{\sigma}^e(\boldsymbol{A}^{DC})\right)\Big|_{\partial\Omega_c}^+ \boldsymbol{n} \qquad \text{on } \partial\Omega_c, \tag{8k}$$

where we have assumed a similar decomposition of the Dirichlet displacement condition $\boldsymbol{u}^D = \boldsymbol{u}^D_{DC} + \boldsymbol{u}^D_{AC}(t)$.

3. LINEARISATION

With developing a FE framework for the approximate solution of (7) and (8) in mind, we linearise weighted residual statements of the transmission problems. To this end, it is convenient to introduce the following

$$X := \{\boldsymbol{A} \in \boldsymbol{H}(\text{curl}, \mathbb{R}^3) : \nabla \cdot \boldsymbol{A} = 0 \quad \text{in } \mathbb{R}^3\backslash\Omega_c\},$$

$$Y(\boldsymbol{g}) := \{\boldsymbol{u} \in H^1(\Omega_c)^3 : \boldsymbol{u} = \boldsymbol{g} \quad \text{on } \partial\Omega_c^D\},$$

$$Z := \{\hat{p} \in H^1(\mathbb{R}^3\backslash\Omega_c)\},$$

which will be used to describe the weak solutions to the dynamic and static transmission problems, where $\boldsymbol{H}(\text{curl}, \mathbb{R}^3)$ and $H^1(\mathbb{R}^3)$ have their usual definitions (e.g. [34]). We start with the treatment of the simpler static problem (8) and then continue to our approach for the transient system (7).
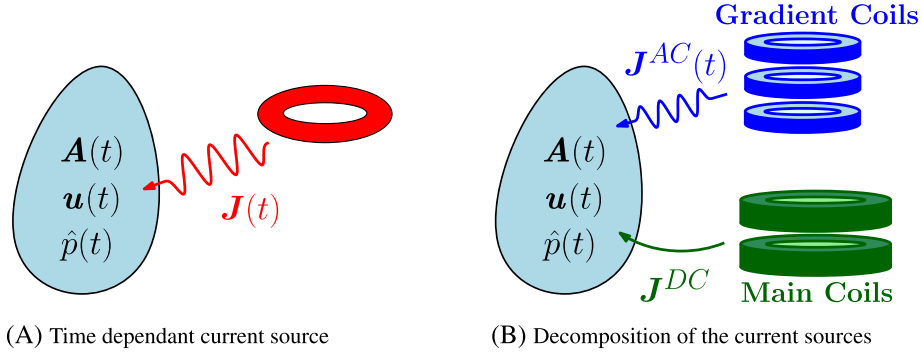
(A) Time dependant current source (B) Decomposition of the current sources

Figure 5. Current source decomposition.

3.1. Linearisation of the static problem

Consider possible weak solutions $(\boldsymbol{A}^{DC}, \boldsymbol{u}^{DC}, \hat{p}^{DC}) \in X \times Y(\boldsymbol{u}^D_{DC}) \times Z$ and the associated residuals

$$R_A^{DC}(\boldsymbol{A}^{\delta}; \boldsymbol{A}^{DC}) := \int_{\mathbb{R}^3} (\mu^{-1} \nabla \times \boldsymbol{A}^{DC} \cdot \nabla \times \boldsymbol{A}^{\delta}) \mathrm{d}\Omega - \int_{\mathbb{R}^3} \boldsymbol{J}^{DC} \cdot \boldsymbol{A}^{\delta} \mathrm{d}\Omega, \tag{9a}$$

$$R_u^{DC}(\boldsymbol{u}^{\delta}; \boldsymbol{A}^{DC}, \boldsymbol{u}^{DC}, \hat{p}^{DC}) := \int_{\Omega_c} (\boldsymbol{\sigma}^m(\boldsymbol{u}^{DC}) + \boldsymbol{\sigma}^e(\boldsymbol{A}^{DC})) : \nabla \boldsymbol{u}^{\delta} \mathrm{d}\Omega$$
$$- \int_{\partial\Omega_c^N} (\hat{p}\boldsymbol{I} + \boldsymbol{\sigma}^e)|^+_- \boldsymbol{n}^- \cdot \boldsymbol{u}^{\delta} \mathrm{d}s, \tag{9b}$$

$$R_{\hat{p}}^{DC}(\hat{p}^{\delta}; \boldsymbol{A}^{DC}, \hat{p}^{DC}) := \int_{\mathbb{R}^3 \backslash \Omega_c} (\nabla \hat{p}^{DC} \cdot \nabla \hat{p}^{\delta} + (\nabla \cdot \boldsymbol{\sigma}^e) \cdot \nabla \hat{p}^{\delta}) \mathrm{d}\Omega, \tag{9c}$$

for all $(\boldsymbol{A}^{\delta}, \boldsymbol{u}^{\delta}, \hat{p}^{\delta}) \in X \times Y(\boldsymbol{0}) \times Z$. The directional derivatives of these residuals are

$$DR_A^{DC}(\boldsymbol{A}^{\delta}; \boldsymbol{A}^{DC})[\boldsymbol{\delta}_A^{DC}] = \int_{\mathbb{R}^3} (\mu^{-1} \nabla \times \boldsymbol{\delta}_A^{DC} \cdot \nabla \times \boldsymbol{A}^{\delta}) \mathrm{d}\Omega, \tag{10a}$$

$$DR_u^{DC}(\boldsymbol{u}^{\delta}; \boldsymbol{A}^{DC}, \boldsymbol{u}^{DC}, \hat{p}^{DC})[\boldsymbol{\delta}_A^{DC}] = \int_{\Omega_c} \mu^{-1} \mathcal{S}(\boldsymbol{A}^{DC}, \boldsymbol{\delta}_A^{DC}) : \nabla \boldsymbol{u}^{\delta} \mathrm{d}\Omega$$
$$- \int_{\partial\Omega_c^N} \mu_0^{-1} \mathcal{S}(\boldsymbol{A}^{DC}, \boldsymbol{\delta}_A^{DC})|^+_- \boldsymbol{n}^- \cdot \boldsymbol{u}^{\delta} \mathrm{d}s, \tag{10b}$$

$$DR_u^{DC}(\boldsymbol{u}^{\delta}; \boldsymbol{A}^{DC}, \boldsymbol{u}^{DC}, \hat{p}^{DC})[\boldsymbol{\delta}_u^{DC}] = \int_{\Omega_c} \boldsymbol{\sigma}^m(\boldsymbol{\delta}_u^{DC}) : \nabla \boldsymbol{u}^{\delta} \mathrm{d}\Omega, \tag{10c}$$

$$DR_u^{DC}(\boldsymbol{u}^{\delta}; \boldsymbol{A}^{DC}, \boldsymbol{u}^{DC}, \hat{p}^{DC})[\boldsymbol{\delta}_{\hat{p}}^{DC}] = - \int_{\partial\Omega_c^N} \boldsymbol{\delta}_{\hat{p}}^{DC}|^+_- \boldsymbol{n}^- \cdot \boldsymbol{u}^{\delta} \mathrm{d}s, \tag{10d}$$

$$DR_{\hat{p}}^{DC}(\hat{p}^{\delta}; \boldsymbol{A}^{DC}, \hat{p}^{DC},)[\boldsymbol{\delta}_A^{DC}] = - \int_{\mathrm{supp}(\boldsymbol{J}^{DC})} ((\nabla \times \boldsymbol{\delta}_A^{DC}) \times \boldsymbol{J}^{DC}) \cdot \nabla \hat{p}^{\delta} \mathrm{d}\Omega, \tag{10e}$$

$$DR_{\hat{p}}^{DC}(\hat{p}^{\delta}; \boldsymbol{A}^{DC}\hat{p}^{DC})[\boldsymbol{\delta}_{\hat{p}}^{DC}] = \int_{\mathbb{R}^3 \backslash \Omega_c} \nabla \boldsymbol{\delta}_{\hat{p}}^{DC} \cdot \nabla \hat{p}^{\delta} \mathrm{d}\Omega, \tag{10f}$$

where $\boldsymbol{n} = \boldsymbol{n}^+ = \boldsymbol{n}^-$ and we have introduced the linearised electromagnetic stress tensor

$$\mathcal{S}(\boldsymbol{A}^{DC}, \boldsymbol{\delta}_A^{DC}) := \nabla \times \boldsymbol{A}^{DC} \otimes \nabla \times \boldsymbol{\delta}_A^{DC} + \nabla \times \boldsymbol{\delta}_A^{DC} \otimes \nabla \times \boldsymbol{A}^{DC} - \left(\nabla \times \boldsymbol{A}^{DC} \cdot \nabla \times \boldsymbol{\delta}_A^{DC} \right) \boldsymbol{I}.$$

At a continuous level, equations (9,10) can be used to introduce the Newton–Raphson iteration: Find $(\boldsymbol{\delta}_A^{DC[m]}, \boldsymbol{\delta}_u^{DC[m]}, \delta_{\hat{p}}^{DC[m]}) \in X \times Y(\boldsymbol{0}) \times Z$ such that

$$DR_A^{DC}(\boldsymbol{A}^\delta; \boldsymbol{A}^{DC[m]})[\boldsymbol{\delta}_A^{DC[m]}] = -R_A^{DC}(\boldsymbol{A}^\delta; \boldsymbol{A}^{DC[m]}), \tag{11a}$$

$$DR_u^{DC}(\boldsymbol{u}^\delta; \boldsymbol{A}^{DC[m]}, \boldsymbol{u}^{DC[m]}, \hat{p}^{DC[m]})[\boldsymbol{\delta}_A^{DC[m]}]+$$
$$DR_u^{DC}(\boldsymbol{u}^\delta; \boldsymbol{A}^{DC[m]}, \boldsymbol{u}^{DC[m]}, \hat{p}^{DC[m]})[\boldsymbol{\delta}_u^{DC[m]}]+$$
$$DR_u^{DC}(\boldsymbol{u}^\delta; \boldsymbol{A}^{DC[m]}, \boldsymbol{u}^{DC[m]}, \hat{p}^{DC[m]})[\delta_{\hat{p}}^{DC[m]}] = -R_u^{DC}(\boldsymbol{u}^\delta; \boldsymbol{A}^{DC[m]}, \boldsymbol{u}^{DC[m]}, \hat{p}^{DC[m]}), \tag{11b}$$

$$DR_{\hat{p}}^{DC}(\hat{p}^\delta; \boldsymbol{A}^{DC[m]}, \hat{p}^{DC[m]})[\boldsymbol{\delta}_A^{DC[m]}]+$$
$$DR_{\hat{p}}^{DC}(\hat{p}^\delta; \boldsymbol{A}^{DC}, \hat{p}^{DC[m]})[\delta_{\hat{p}}^{DC[m]}] = -R_{\hat{p}}^{DC}(\hat{p}^\delta; \boldsymbol{A}^{DC[m]}, \hat{p}^{DC[m]}), \tag{11c}$$

for all $(\boldsymbol{A}^\delta, \boldsymbol{u}^\delta, \hat{p}^\delta) \in X \times Y(\boldsymbol{0}) \times Z$ where

$$\boldsymbol{A}^{DC[m+1]} = \boldsymbol{A}^{DC[m]} + \boldsymbol{\delta}_A^{DC[m]},$$
$$\boldsymbol{u}^{DC[m+1]} = \boldsymbol{u}^{DC[m]} + \boldsymbol{\delta}_u^{DC[m]},$$
$$\hat{p}^{DC[m+1]} = \hat{p}^{DC[m]} + \delta_{\hat{p}}^{DC[m]}.$$

The initial guesses are such that $(\boldsymbol{A}^{DC[0]}, \boldsymbol{u}^{DC[0]}, \hat{p}^{DC[0]}) \in (X \times Y(\boldsymbol{u}_{DC}^D) \times Z)$. To permit the computational solution of (11), a spatial FE discretisation is required, which we will discuss in Section 4. However, at this stage, it is already useful to note that, because of the specific nature of the equations, (11a) can be solved independently, followed by (11c) and then (11b) without iteration. Moreover, if the system is solved monolithically, the solution will converge to $(\boldsymbol{A}^{DC}, \boldsymbol{u}^{DC}, \hat{p}^{DC}) \in (X \times Y(\boldsymbol{u}_{DC}^D) \times Z)$ in a single iteration.

In our previous approach [2], we neglected the effects of the static displacement, driven by the static magnetic field, as we were primarily interested in computing the output power of the system that depends only upon the transient displacements, which were assumed to be harmonic. However, in this new formulation, we also include the static effects of the displacements to allow for a rigorous treatment of the linearised transient scheme and maintain consistency of the physical fields.

3.2. Linearisation of the dynamic problem

Consider possible transient weak solutions $(\boldsymbol{A}, \boldsymbol{u}, \hat{p})(t) \in (X \times Y(\boldsymbol{u}_{AC}^D) \times Z)[0, T]$ and the associated residuals

$$R_A(\boldsymbol{A}^\delta; \boldsymbol{A}, \boldsymbol{u}) := \int_{\mathbb{R}^3} \left(\mu^{-1} \nabla \times \boldsymbol{A} \cdot \nabla \times \boldsymbol{A}^\delta + \gamma \frac{\partial \boldsymbol{A}}{\partial t} \cdot \boldsymbol{A}^\delta \right) d\Omega - \int_{\mathbb{R}^3} \boldsymbol{J}^s \cdot \boldsymbol{A}^\delta d\Omega$$
$$- \int_{\Omega_c} \gamma \frac{\partial \boldsymbol{u}}{\partial t} \times (\nabla \times \boldsymbol{A}) \cdot \boldsymbol{A}^\delta d\Omega, \tag{12a}$$

$$R_u(\boldsymbol{u}^\delta; \boldsymbol{A}, \boldsymbol{u}, \hat{p}) := \int_{\Omega_c} (\boldsymbol{\sigma}^m(\boldsymbol{u}) + \boldsymbol{\sigma}^e(\boldsymbol{A})) : \nabla \boldsymbol{u}^\delta d\Omega + \int_{\Omega_c} \rho \frac{\partial^2 \boldsymbol{u}}{\partial t^2} \cdot \boldsymbol{u}^\delta d\Omega$$
$$- \int_{\partial \Omega_c^N} (\hat{p}\boldsymbol{I} + \boldsymbol{\sigma}^e(\boldsymbol{A}))|^+ \boldsymbol{n}^- \cdot \boldsymbol{u}^\delta ds, \tag{12b}$$

$$R_{\hat{p}}(\hat{p}^\delta; \boldsymbol{A}, \boldsymbol{u}, \hat{p}) := \int_{\mathbb{R}^3 \backslash \Omega_c} \left(\nabla \hat{p} \cdot \nabla \hat{p}^\delta + \frac{1}{c^2} \frac{\partial^2 \hat{p}}{\partial t^2} \cdot p^\delta + \nabla \cdot \boldsymbol{\sigma}^e \cdot \nabla \hat{p}^\delta \right) d\Omega$$
$$- \int_{\partial \Omega_c^N} \rho^+ \frac{\partial^2 \boldsymbol{u}}{\partial t^2} \bigg|^- \cdot \boldsymbol{n}^+ p^\delta ds, \tag{12c}$$

for all $(A^\delta, u^\delta, \hat{p}^\delta) \in (X \times Y(\mathbf{0}) \times Z)$. The directional derivatives of these residuals are

$$
DR_A(A^\delta; A, u)[\delta_A] = \int_{\mathbb{R}^3} \left(\mu^{-1} \nabla \times \delta_A \cdot \nabla \times A^\delta + \gamma \frac{\partial \delta_A}{\partial t} \cdot A^\delta \right) \mathrm{d}\Omega
$$
$$
- \int_{\Omega_c} \left(\gamma \frac{\partial u}{\partial t} \times (\nabla \times \delta_A) \right) \cdot A^\delta \mathrm{d}\Omega, \tag{13a}
$$

$$
DR_A(A^\delta; A, u)[\delta_u] = - \int_{\Omega_c} \left(\gamma \frac{\partial \delta_u}{\partial t} \times (\nabla \times A) \cdot A^\delta \right) \mathrm{d}\Omega, \tag{13b}
$$

$$
DR_u(u^\delta; A, u, \hat{p})[\delta_A] = \int_{\Omega_c} \mu^{-1} \mathcal{S}(A, \delta_A) : \nabla u^\delta \mathrm{d}\Omega
$$
$$
- \int_{\partial \Omega_c^N} \mu_0^{-1} \mathcal{S}(A, \delta_A)|^+ n^- \cdot u^\delta \mathrm{d}s, \tag{13c}
$$

$$
DR_u(u^\delta; A, u, \hat{p})[\delta_u] = \int_{\Omega_c} \left(\sigma^m(\delta_u) : \nabla u^\delta + \rho \frac{\partial^2 \delta_u}{\partial t^2} \cdot u^\delta \right) \mathrm{d}\Omega, \tag{13d}
$$

$$
DR_u(u^\delta; A, u, \hat{p})[\delta_{\hat{p}}] = - \int_{\partial \Omega_c^N} \delta_{\hat{p}}|^+ n^- \cdot u^\delta \mathrm{d}s, \tag{13e}
$$

$$
DR_{\hat{p}}(\hat{p}^\delta; A, u, \hat{p})[\delta_A] = - \int_{\mathrm{supp}(J^s)} \left(\nabla \times \delta_A \times (\nabla \times (\mu_0^{-1} \nabla \times A)) \right.
$$
$$
\left. + \nabla \times A \times (\nabla \times (\mu_0^{-1} \nabla \times \delta_A)) \right) \cdot \nabla \hat{p}^\delta \mathrm{d}\Omega, \tag{13f}
$$

$$
DR_{\hat{p}}(\hat{p}^\delta; A, u, \hat{p})[\delta_u] = - \int_{\partial \Omega_c^N} \rho^+ \frac{\partial^2 \delta_u}{\partial t^2} \bigg|^- \cdot n^+ \hat{p}^\delta \mathrm{d}s, \tag{13g}
$$

$$
DR_{\hat{p}}(\hat{p}^\delta; A, u, \hat{p})[\delta_{\hat{p}}] = \int_{\mathbb{R}^3 \backslash \Omega_c} \left(\nabla \delta_{\hat{p}} \cdot \nabla \hat{p}^\delta + \frac{1}{c^2} \frac{\partial^2 \delta_{\hat{p}}}{\partial t^2} \cdot \hat{p}^\delta \right) \mathrm{d}\Omega. \tag{13h}
$$

In the preceding equations, we have found it convenient to use the alternative form of $\nabla \cdot \sigma^e$ introduced in (5) when linearising $R_{\hat{p}}$.

One strategy for solving the temporal system, after spatial discretisation, would be to adopt a discrete time integration scheme and then apply the Newton–Raphson algorithm at each time-step to solve the non-linear equations using the directional derivatives computed previously. However, such an approach is computationally expensive and, in the interests of developing a fast computational technique, we adopt a different strategy.

Rather than integrating the equations in time and solving the non-linear equations at each time step, we choose instead to linearise the full time dependant equations about the static solution. This linearisation in the context of MRI scanners is motivated by the knowledge that the static DC current source is several orders of magnitude stronger than the weaker AC time varying source, leading to a strong DC field and a weaker time varying field. Similar techniques, involving the additive split of a non-linear problem to a series of linear problems, have been successfully applied to the field of computational mechanics such as analysis of structural membranes [35–37], high-order mesh generation [38] and in biomedical applications [39]. In this case, the residuals of the dynamic problem become

$$
\tilde{R}_A^{AC}(A^\delta) := R_A(A^\delta; A^{DC}, u^{DC}) = - \int_{\mathrm{supp}(J^{AC})} J^{AC} \cdot A^\delta \mathrm{d}\Omega, \tag{14a}
$$

$$
\tilde{R}_A^{AC}(u^\delta) := R_u(u^\delta; A^{DC}, u^{DC}, \hat{p}^{DC}) = 0, \tag{14b}
$$

$$
\tilde{R}_{\hat{p}}^{AC}(\hat{p}^\delta) := R_{\hat{p}}(\hat{p}^\delta; A^{DC}, u^{DC}, \hat{p}^{DC}) = - \int_{\mathrm{supp}(J^{AC})} ((\nabla \times A^{DC}) \times J^{AC}) \cdot \nabla \hat{p}^\delta \mathrm{d}\Omega, \tag{14c}
$$

and the associated directional derivatives take the form

$$D\tilde{R}_A^{AC}(A^\delta)[\delta_A] := DR_A(A^\delta; A^{DC}, u^{DC})[\delta_A]$$

$$= \int_{\mathbb{R}^3} \left(\mu^{-1} \nabla \times \delta_A \cdot \nabla \times A^\delta + \gamma \frac{\partial \delta_A}{\partial t} \cdot A^\delta \right) d\Omega, \tag{15a}$$

$$D\tilde{R}_A^{AC}(A^\delta; A^{DC})[\delta_u] := DR_A(A^\delta; A^{DC}, u^{DC})[\delta_u] = -\int_{\Omega_c} \gamma \frac{\partial \delta_u}{\partial t} \times (\nabla \times A^{DC}) \cdot A^\delta d\Omega, \tag{15b}$$

$$D\tilde{R}_u^{AC}(u^\delta; A^{DC})[\delta_A] := DR_u(u^\delta; A^{DC}, u^{DC}, \hat{p}^{DC})[\delta_A] = \int_{\Omega_c} \mu^{-1} \mathcal{S}(A^{DC}, \delta_A) : \nabla u^\delta d\Omega$$

$$- \int_{\partial\Omega_c^N} \mu_0^{-1} \mathcal{S}(A^{DC}, \delta_A)|^+ n^- \cdot u^\delta ds, \tag{15c}$$

$$D\tilde{R}_u^{AC}(u^\delta)[\delta_u] := DR_u(u^\delta; A^{DC}, u^{DC}, \hat{p}^{DC})[\delta_u]$$

$$= \int_{\Omega_c} \left(\sigma^m(\delta_u) : \nabla u^\delta + \rho \frac{\partial^2 \delta_u}{\partial t^2} \cdot u^\delta \right) d\Omega, \tag{15d}$$

$$D\tilde{R}_u^{AC}(u^\delta)[\delta_{\hat{p}}] := DR_u(u^\delta; A^{DC}, u^{DC}, \hat{p}^{DC})[\delta_{\hat{p}}] = -\int_{\partial\Omega_c^N} \delta_{\hat{p}}|^+ n^- \cdot u^\delta ds, \tag{15e}$$

$$D\tilde{R}_{\hat{p}}^{AC}(\hat{p}^\delta; A^{DC})[\delta_A] := DR_{\hat{p}}(\hat{p}^\delta; A^{DC}, \hat{p}^{DC})[\delta_A] = -\int_{\text{supp}(J^{DC})} \left((\nabla \times \delta_A) \times J^{DC} \right) \cdot \nabla \hat{p}^\delta d\Omega$$

$$- \int_{\text{supp}(J^{DC}) \cup \text{supp}(J^{AC})} \left(\nabla \times A^{DC} \times (\nabla \times (\mu_0^{-1} \nabla \times \delta_A)) \right) \cdot \nabla \hat{p}^\delta d\Omega, \tag{15f}$$

$$D\tilde{R}_{\hat{p}}^{AC}(\hat{p}^\delta)[\delta_u] := DR_{\hat{p}}(\hat{p}^\delta; A^{DC}, u^{DC}, \hat{p}^{DC})[\delta_u] = -\int_{\partial\Omega_c^N} \rho^+ \frac{\partial^2 \delta_u}{\partial t^2} \bigg|^- \cdot n^+ \hat{p}^\delta ds, \tag{15g}$$

$$D\tilde{R}_{\hat{p}}^{AC}(\hat{p}^\delta)[\delta_{\hat{p}}] := DR_{\hat{p}}(\hat{p}^\delta; A^{DC}, \hat{p}^{DC})[\delta_{\hat{p}}] = \int_{\mathbb{R}^3 \setminus \Omega_c} \left(\nabla \delta_{\hat{p}} \cdot \nabla \hat{p}^\delta + \frac{1}{c^2} \frac{\partial^2 \delta_{\hat{p}}}{\partial t^2} \cdot \hat{p}^\delta \right) d\Omega. \tag{15h}$$

Finally, recalling that $A^{DC}, u^{DC}, \hat{p}^{DC}$ are all time invariant, we see that the residuals and the directional derivatives in (14) and (15), respectively, are linear in the time dependent terms $\delta_A, \delta_u, \delta_{\hat{p}}$ and J^{AC}. This motivates the time harmonic representations

$$\delta_A \rightarrow \delta_A e^{i\omega t},$$
$$\delta_u \rightarrow \delta_u e^{i\omega t},$$
$$\delta_{\hat{p}} \rightarrow \delta_{\hat{p}} e^{i\omega t},$$
$$J^{AC} \rightarrow J^{AC} e^{i\omega t},$$

where ω denotes the angular frequency of the driving current in the gradient coils in the case of a harmonic excitation. In reality, the gradient coils are driven using non-harmonic excitations, but their time signals can be decomposed into its different frequency modes and the same approach applied. The solution of the linear harmonic problem becomes as follows: find $(\delta_A, \delta_u, \delta_{\hat{p}}) \in X \times Y(u_{AC}^D) \times Z$ such that

$$D\tilde{R}_A^{AC}(A^\delta)[\delta_A] + D\tilde{R}_A^{AC}(A^\delta; A^{DC})[\delta_u] = -\tilde{R}_A^{AC}(A^\delta)$$

$$= \int_{\text{supp}(J^{AC})} J^{AC} \cdot A^\delta d\Omega, \tag{16a}$$

$$D\tilde{R}_u^{AC}(u^\delta; A^{DC})[\delta_A] + D\tilde{R}_u^{AC}(u^\delta)[\delta_u] + D\tilde{R}_u^{AC}(u^\delta)[\delta_{\hat{p}}] = -\tilde{R}_u^{AC}(u^\delta)$$

$$= 0, \tag{16b}$$

$$D\tilde{R}_{\hat{p}}^{AC}(\hat{p}^\delta; A^{DC})[\delta_A] + D\tilde{R}_{\hat{p}}^{AC}(\hat{p}^\delta)[\delta_u] + D\tilde{R}_{\hat{p}}^{AC}(\hat{p}^\delta)[\delta_{\hat{p}}] = -\tilde{R}_{\hat{p}}^{AC}(\hat{p}^\delta)$$

$$= \int_{\text{supp}(J^{AC})} (\nabla \times A^{DC}) \times J^{AC} \cdot \nabla \hat{p}^\delta d\Omega. \tag{16c}$$

for all $(A^\delta, u^\delta, \hat{p}^\delta) \in X \times Y(0) \times Z$ where it assumed that $u_{AC}^D \to u_{AC}^D e^{i\omega t}$. We may then decompose the full temporal solution into its static and time varying components, which in the case of a single frequency excitation are given by

$$A(t) = A^{DC} + \mathrm{Re}(\delta_A e^{i\omega t}),$$
$$u(t) = u^{DC} + \mathrm{Re}(\delta_u e^{i\omega t}),$$
$$\hat{p}(t) = \hat{p}^{DC} + \mathrm{Re}(\delta_{\hat{p}} e^{i\omega t}).$$

The directional derivatives in Equation (16) explicitly become

$$D\tilde{R}_A^{AC}(A^\delta)[\delta_A] = \int_{\mathbb{R}^3} \left(\mu^{-1} \nabla \times \delta_A \cdot \nabla \times A^\delta + i\omega\gamma \delta_A \cdot A^\delta \right) d\Omega, \tag{17a}$$

$$D\tilde{R}_A^{AC}(A^\delta; A^{DC})[\delta_u] = -\int_{\Omega_c} i\omega\gamma \delta_u \times (\nabla \times A^{DC}) \cdot A^\delta d\Omega, \tag{17b}$$

$$D\tilde{R}_u^{AC}(u^\delta; A^{DC})[\delta_A] = \int_{\Omega_c} \mu^{-1} \mathcal{S}(A^{DC}, \delta_A) : \nabla u^\delta d\Omega$$
$$- \int_{\partial\Omega_c^N} \mu_0^{-1} \mathcal{S}(A^{DC}, \delta_A)|^+ n^- \cdot u^\delta ds, \tag{17c}$$

$$D\tilde{R}_u^{AC}(u^\delta)[\delta_u] = \int_{\Omega_c} \left(\sigma^m(\delta_u) : \nabla u^\delta - \rho\omega^2 \delta_u \cdot u^\delta \right) d\Omega, \tag{17d}$$

$$D\tilde{R}_u^{AC}(u^\delta)[\delta_{\hat{p}}] = -\int_{\partial\Omega_c^N} \delta_{\hat{p}}|^+ n^- \cdot u^\delta ds, \tag{17e}$$

$$D\tilde{R}_{\hat{p}}^{AC}(\hat{p}^\delta; A^{DC})[\delta_A] = -\int_{\mathrm{supp}(J^{DC})} \left((\nabla \times \delta_A) \times J^{DC} \right) \cdot \nabla\hat{p}^\delta d\Omega$$
$$- \int_{\mathrm{supp}(J^{DC})\cup\mathrm{supp}(J^{AC})} \left(\nabla \times A^{DC} \times (\nabla \times (\mu_0^{-1}\nabla \times \delta_A)) \right) \cdot \nabla\hat{p}^\delta d\Omega, \tag{17f}$$

$$D\tilde{R}_{\hat{p}}^{AC}(\hat{p}^\delta)[\delta_u] = \int_{\partial\Omega_c^N} \omega^2 \rho^+ \delta_u|^- \cdot n^+ \hat{p}^\delta ds, \tag{17g}$$

$$D\tilde{R}_{\hat{p}}^{AC}(\hat{p}^\delta)[\delta_{\hat{p}}] = \int_{\mathbb{R}^3\setminus\Omega_c} \left(\nabla\delta_{\hat{p}} \cdot \nabla\hat{p}^\delta - \frac{\omega^2}{c^2}\delta_{\hat{p}} \cdot \hat{p}^\delta \right) d\Omega. \tag{17h}$$

In the absence of pressure, the formulation previously proposed in [2] for the dynamic case is identical to that obtained in the preceding equations; however, previously, a number of assumptions had to be made in order to drop terms to arrive at the considered system, which is now no longer the case. Moreover, in the preceding formulation, the equations are rigorously established through a linearisation of the dynamic system and the solutions can be obtained by a single monolithic solve rather than an iterative fixed point scheme, previously proposed.

4. COMPUTATIONAL TREATMENT

In this section, we discuss the key components for the computational solution to Equations (16) and (11). This includes the reduction for rotationally symmetric geometries in Section 4.1, the far field treatment in Section 4.2 and the hp–FE discretisation in Section 4.3.

4.1. Reduction for rotationally symmetric geometries

The formulation proposed in Section 3 is valid for general three-dimensional domains involving a conducting region surrounded by an unbounded region of free space containing the current sources.

To a first approximation, the geometry of an MRI scanner is close to cylindrical and the strong DC current source $\boldsymbol{J}^{DC}$ has only the component J_ϕ^{DC} in cylindrical coordinates (r, ϕ, z). However, of the three sets of AC gradient coils, it is only the z-gradient coil that exhibits rotational symmetry, and in our quest for a rapid industrial design tool, we must neglect the x and y gradient coils. Under these assumptions, our simplified MRI scanner is rotationally symmetric with respect to the azimuth, the problem reduces to solving for $\boldsymbol{A} = A_\phi(r, z)\boldsymbol{e}_\phi$, $\boldsymbol{u} = u_r(r, z)\boldsymbol{e}_r + u_z(r, z)\boldsymbol{e}_z$, $\hat{p} = \hat{p}(r, z)$ [2]. Here $\boldsymbol{e}_r$, $\boldsymbol{e}_\phi$ and $\boldsymbol{e}_z$ denote the standard basis of the cylindrical coordinate system. The reduction of the full three-dimensional problem to the axisymmetric meridian (r, z) plane Ω^m is shown in Figure 6. However, by projection of this plane, full three-dimensional results are still achieved.

When transformed to the axisymmetric domain, the spaces in which the weak solutions are sought in the variational statements (16) and (11) must also be adapted. In general, this leads to necessity to seek for solutions in weighted spaces to ensure the fields are well behaved at the radial axis [40]. To avoid the complexity of weighted spaces, we transform the fields $A_\phi = r\hat{A}_\phi$ and $u_r = r\hat{u}_r$ according to that proposed in [2], and note that $\hat{A}_\phi \in H^1(\Omega^m)$, $\tilde{\boldsymbol{u}} := [\hat{u}_r, u_z] \in H^1(\Omega^m)$. The acoustic pressure presents no difficulty because $\hat{p}(r, z) \in H^1(\Omega^m)$. The treatment of the bilinear and linear forms associated with the terms in (11) and (16) follow similar steps to that presented in [2], and hence, we only give as an example

$$D\tilde{R}_{\hat{p}}^{AC}(\hat{p}^\delta)[\delta_{\hat{p}}] = 2\pi \int_{\mathbb{R}^2 \backslash \Omega_c^m} \left(\nabla_m \delta_{\hat{p}} \cdot \nabla_m \hat{p}^\delta - \frac{\omega^2}{c^2} \delta_{\hat{p}} \cdot \hat{p}^\delta \right) r \, \mathrm{d}\Omega^m, \tag{18}$$

where Ω_c^m is the projection of Ω_c on to the meridian plane, $\nabla_m := [\partial/\partial r, \partial/\partial z]^T$ and the factor of 2π results from the integration of the azimuthal direction. This factor similarly appears in the treatment of all of the other terms in the linear system and therefore cancels.

4.2. Far field treatment

The strong forms of the dynamic and static problems include radiation and decay conditions, which describe the behaviour of $\boldsymbol{A}$, $\boldsymbol{A}^{DC}$, $\hat{p}$ and $\hat{p}^{DC}$ as $|\boldsymbol{x}| \to \infty$. To allow the computational treatment of the problem, the unbounded free space region $\mathbb{R}^3 \backslash \Omega_c$ is truncated at a finite distance from Ω_c and the region Ω_n is created, which contains all the current sources. The three-dimensional computational domain $\Omega := \Omega_n \cup \Omega_c \subset \mathbb{R}^3$ becomes $\Omega^m := \Omega_n^m \cup \Omega_c^m \subset \mathbb{R}^2$ for axisymmetric problems. This means that integrals over $\mathbb{R}^3 \backslash \Omega_c$ in (11) and (16) become integrals over Ω_n and then, in turn, Ω_n^m. On $\partial\Omega^m$, the static decay of $\boldsymbol{A}$, $\boldsymbol{A}^{DC}$, $\hat{p}^{DC}$ is approximated by fixing $\partial\Omega^m$ to be located sufficiently far from the region of interest and setting

$$\boldsymbol{A} = \boldsymbol{A}^{DC} = A_\phi \boldsymbol{e}_\phi = A_\phi^{DC} \boldsymbol{e}_\phi = \boldsymbol{0},$$
$$\hat{p}^{DC} = 0 \qquad \text{on } \partial\Omega^m.$$

Naturally, the quality of the approximation improves as the size of Ω_n (Ω_n^m) is increased. However, the harmonic pressure field, and in particular the treatment of $D\tilde{R}_{\hat{p}}^{AC}(\hat{p}^\delta)[\delta_{\hat{p}}]$, cannot merely be approximated by truncating the domain and fixing $\hat{p} = 0$ at $\partial\Omega^m$, because this would result in reflections that
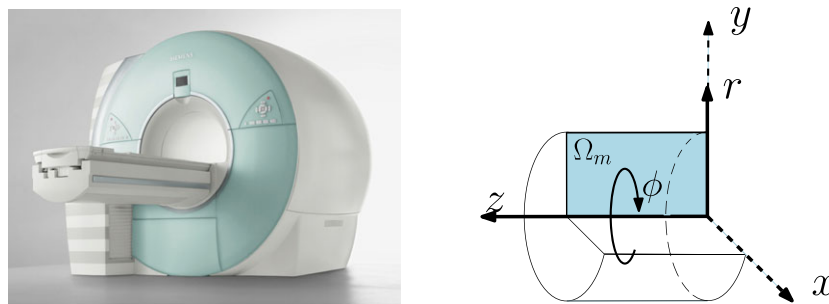

Figure 6. Transformation from three-dimensional full scanner to simplified 2D axisymmetric case.

would pollute the computational domain because of its wave behaviour. The radiation condition (4) in the continuous problem describes the correct decay of this field, which must also be approximated computationally. Therefore, we add a PML [32] Ω_{pml} (Ω_{pml}^m) to the exterior of Ω_n (Ω_n^m) so that the computational domain now becomes $\Omega = \Omega_c \cup \Omega_n \cup \Omega_{pml}$ ($\Omega^m = \Omega_c^m \cup \Omega_n^m \cup \Omega_{pml}^m$). For terms other than $D\tilde{R}_{\hat{p}}^{AC}(\hat{p}^\delta)[\delta_{\hat{p}}]$ in (16), Ω_{pml} can be merely thought of as a free space extension of Ω_n. However, the aforementioned term (18) is treated differently as

$$
\begin{aligned}
D\tilde{R}_{\hat{p}}^{AC}(\hat{p}^\delta)[\delta_{\hat{p}}] = &\int_{\Omega_n^m} \left(\nabla_m \delta_{\hat{p}} \cdot \nabla_m \hat{p}^\delta - \frac{\omega^2}{c^2} \delta_{\hat{p}} p^\delta \right) r \, \mathrm{d}\Omega_m \\
&+ \int_{\Omega_{pml}^m} \left(\mathbf{\Lambda}_1 \nabla_m \delta_{\hat{p}} \cdot \nabla_m \hat{p}^\delta - \frac{\omega^2}{c^2} \Lambda_2 \delta_{\hat{p}} p^\delta \right) r \, \mathrm{d}\Omega_m,
\end{aligned}
\tag{19}
$$

where $\mathbf{\Lambda}_1$, Λ_2 are both complex functions of position in the layer and reduce to identity on $\partial\Omega_n^m \cap \partial\Omega_{pml}^m$. The coefficients of these functions can be established through a complex coordinate stretching of the domain Ω_n^m following the approach in [32]. For the axisymmetric case, this complex stretching is equivalent to introducing the complex position-dependent functions

$$
\mathbf{\Lambda}_1 = \frac{1}{r} \begin{bmatrix} \frac{z_z' z_r}{z_r'} & 0 \\ 0 & \frac{z_r' z_r}{z_z'} \end{bmatrix}, \qquad \Lambda_2 = \frac{z_r' z_z' z_r}{r}.
$$

In the preceding equation, the complex coordinate transform z_s is described as a power law in terms of the distance to the layer d_s and thickness of the layer t_s, as illustrated in Figure 7b. The prime indicates differentiation with respect to the argument, and explicitly, we choose

$$
z_s(s) = \begin{cases} s & 0 \leqslant |s| < d_k \\ s - \mathrm{i}\left(\frac{|s| - d_s}{t_s} \right)^5 s & |s| \geqslant d_k \end{cases},
$$

where $s = [r, z]$. The choice of a power law of degree 5 and user-defined thickness t_s is somewhat arbitrary, provided that the resulting complex field behaviour in Ω_{pml}^m is properly resolved. If this is accomplished, the acoustic pressure field is absorbed without reflection and we can set $\hat{p} = 0$ on $\partial\Omega^m$.

4.3. hp−FE discretisation

Building on the previous success in [2], we choose to adopt the hp−FE H^1 conforming basis functions, proposed by Zaglmayr and Schöberl [41,42], for accurately discretising the fields $\hat{A}_\phi$, $\tilde{u}$

(A) Effect of complex coordinate stretching
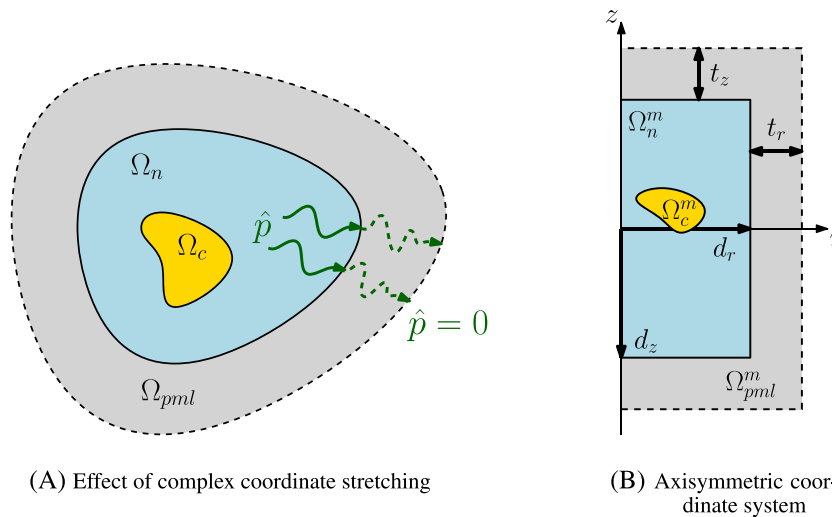
(B) Axisymmetric coordinate system

Figure 7. Representation of the perfectly matched layer.

and $\hat{p}$. Denoting their two-dimensional basis function set for triangular grids by X_{hp} the discrete static problem becomes $(\delta_{A_\phi hp}^{DC[m]}\boldsymbol{e}_\phi, \boldsymbol{\delta}_{\tilde{u}hp}^{DC[m]}, \delta_{\hat{p}hp}^{DC[m]}) = (r\delta_{\hat{A}_\phi hp}^{DC[m]}\boldsymbol{e}_\phi, r\delta_{\hat{u}_r hp}^{DC[m]}\boldsymbol{e}_r + \delta_{u_z hp}^{DC[m]}\boldsymbol{e}_z, \delta_{\hat{p}hp}^{DC[m]}) \in \tilde{X}(\boldsymbol{0}) \cap rX_{hp}\boldsymbol{e}_\phi \times Y(\boldsymbol{0}) \cap (rX_{hp}\boldsymbol{e}_r + X_{hp}\boldsymbol{e}_z) \times \tilde{Z}(0) \cap X_{hp}$ such that

$$DR_A^{DC}(A_{\phi hp}^\delta\boldsymbol{e}_\phi; A_{\phi hp}^{DC[m]}\boldsymbol{e}_\phi)[\delta_{A_\phi hp}^{DC[m]}\boldsymbol{e}_\phi] = -R_A^{DC}(A_{\phi hp}^\delta\boldsymbol{e}_\phi; A_{\phi hp}^{DC[m]}\boldsymbol{e}_\phi), \tag{20a}$$

$$DR_u^{DC}(\tilde{\boldsymbol{u}}_{hp}^\delta; A_{\phi hp}^{DC[m]}\boldsymbol{e}_\phi, \tilde{\boldsymbol{u}}_{hp}^{DC[m]}, \hat{p}_{hp}^{DC[m]})[\delta_{A_\phi hp}^{DC[m]}\boldsymbol{e}_\phi] +$$
$$DR_u^{DC}(\tilde{\boldsymbol{u}}_{hp}^\delta; A_{\phi hp}^{DC[m]}\boldsymbol{e}_\phi, \tilde{\boldsymbol{u}}_{hp}^{DC[m]}, \hat{p}_{hp}^{DC[m]})[\boldsymbol{\delta}_{\tilde{u}hp}^{DC[m]}] +$$
$$DR_u^{DC}(\tilde{\boldsymbol{u}}_{hp}^\delta; A_{\phi hp}^{DC[m]}\boldsymbol{e}_\phi, \tilde{\boldsymbol{u}}_{hp}^{DC[m]}, \hat{p}_{hp}^{DC[m]})[\delta_{\hat{p}hp}^{DC[m]}]$$
$$= -R_u^{DC}(\tilde{\boldsymbol{u}}_{hp}^\delta; A_{\phi hp}^{DC[m]}\boldsymbol{e}_\phi, \tilde{\boldsymbol{u}}_{hp}^{DC[m]}, \hat{p}_{hp}^{DC[m]}), \tag{20b}$$

$$DR_{\hat{p}}^{DC}(\hat{p}_{hp}^\delta; A_{\phi hp}^{DC[m]}\boldsymbol{e}_\phi, \hat{p}_{hp}^{DC[m]})[\delta_{A_\phi hp}^{DC[m]}\boldsymbol{e}_\phi] +$$
$$DR_{\hat{p}}^{DC}(\hat{p}_{hp}^\delta; A_{\phi hp}^{DC}\boldsymbol{e}_\phi, \hat{p}_{hp}^{DC[m]})[\delta_{\hat{p}hp}^{DC[m]}] = -R_{\hat{p}}^{DC}(\hat{p}_{hp}^\delta; A_{\phi hp}^{DC[m]}\boldsymbol{e}_\phi, \hat{p}_{hp}^{DC[m]}), \tag{20c}$$

for all $(A_{\phi hp}^\delta\boldsymbol{e}_\phi, \tilde{\boldsymbol{u}}_{hp}^\delta, \hat{p}_{hp}^\delta) = (r\hat{A}_{\phi hp}^\delta\boldsymbol{e}_\phi, r\hat{u}_{rhp}^\delta\boldsymbol{e}_r + u_{zhp}^\delta\boldsymbol{e}_z, \hat{p}_{hp}^\delta) \in \tilde{X}(\boldsymbol{0}) \cap rX_{hp}\boldsymbol{e}_\phi \times Y(\boldsymbol{0}) \cap (rX_{hp}\boldsymbol{e}_r, X_{hp}\boldsymbol{e}_z) \times$

$\tilde{Z}(\boldsymbol{0}) \cap X_{hp}$. In the above we use

$$\tilde{X}(\boldsymbol{g}) := \{\boldsymbol{A} \in \boldsymbol{H}(\text{curl}, \Omega) : \nabla \cdot \boldsymbol{A} = 0 \quad \text{in } \Omega_n \cup \Omega_{pml}, \boldsymbol{A} = \boldsymbol{g} \text{ on } \partial\Omega\},$$
$$\tilde{Z}(g) := \{\hat{p} \in H^1(\Omega_n \cup \Omega_{pml}), \hat{p} = g \text{ on } \partial\Omega\},$$

to account for the domain truncation introduced in Section 4.2. The corresponding discrete linear harmonic problem for $(\delta_{A_\phi hp}\boldsymbol{e}_\phi, \boldsymbol{\delta}_{\tilde{u}hp}, \delta_{\hat{p}hp}) = (r\delta_{\hat{A}_\phi hp}\boldsymbol{e}_\phi, r\delta_{\hat{u}_r hp}\boldsymbol{e}_r + \delta_{u_z hp}\boldsymbol{e}_z, \delta_{\hat{p}hp}) \in \tilde{X}(\boldsymbol{0}) \cap rX_{hp}\boldsymbol{e}_\phi \times Y(\boldsymbol{u}_{AC}^D) \cap (rX_{hp}\boldsymbol{e}_r + X_{hp}\boldsymbol{e}_z) \times \tilde{Z}(\boldsymbol{0}) \cap X_{hp}$ can be developed analogously. We choose not to give the explicit formulae for the terms because they can be found by following the approach for axisymmetric problems, which we have previously described in [2]. The complete algorithm is summarised in Algorithm 1.

Algorithm 1 Algorithm for the discrete hp–FE solution to linearised acousto-magneto-mechanical coupling in MRI scanners.

1: Prescribe an initial guess $(A^{DC[0]}, \boldsymbol{u}^{DC[0]}, \hat{p}^{DC[0]}) = (A_\phi^{DC[0]}\boldsymbol{e}_\phi, \tilde{\boldsymbol{u}}^{DC[0]}, \hat{p}^{DC[0]}) \in (X \times Y(\boldsymbol{u}_{DC}^D) \times Z)$.

2: Obtain the discrete solutions $(\delta_{A_\phi hp}^{DC[0]}\boldsymbol{e}_\phi, \boldsymbol{\delta}_{\tilde{u}hp}^{DC[0]}, \delta_{\hat{p}hp}^{DC[0]})$ by solving the monolithic system (20).

3: Set the DC solutions to be

$$A_{hp}^{DC} = A_{hp}^{DC[1]} = A_{hp}^{DC[1]}\boldsymbol{e}_\phi = (A_{hp}^{DC[0]} + \delta_{A_\phi hp}^{DC[0]})\boldsymbol{e}_\phi,$$
$$\boldsymbol{u}_{hp}^{DC} = \boldsymbol{u}_{hp}^{DC[1]} = \tilde{\boldsymbol{u}}_{hp}^{DC[1]} = \tilde{\boldsymbol{u}}_{hp}^{DC[0]} + \boldsymbol{\delta}_{\tilde{u}hp}^{DC[0]},$$
$$\hat{p}_{hp}^{DC} = \hat{p}_{hp}^{DC[1]} = \hat{p}_{hp}^{DC[0]} + \delta_{\hat{p}hp}^{DC[0]}.$$

4: Obtain the discrete harmonic AC solutions $(\delta_{A_\phi hp}\boldsymbol{e}_\phi, \boldsymbol{\delta}_{\tilde{u}hp}, \delta_{\hat{p}hp})$.

5: The complete linearised transient solutions are then

$$\boldsymbol{A}_{hp}(t) = (A_{\phi hp}^{DC} + \text{Re}(\delta_{A_\phi hp}e^{i\omega t}))\boldsymbol{e}_\phi,$$
$$\tilde{\boldsymbol{u}}_{hp}(t) = \tilde{\boldsymbol{u}}_{hp}^{DC} + \text{Re}(\boldsymbol{\delta}_{\tilde{u}hp}e^{i\omega t}),$$
$$\hat{p}_{hp}(t) = \hat{p}_{hp}^{DC} + \text{Re}(\delta_{\hat{p}hp}e^{i\omega t}).$$

---

5. NUMERICAL RESULTS

In this section, we present a series of academic and industrial numerical examples in order to demonstrate the capabilities of the presented framework. Firstly, we include examples with analytical solutions to demonstrate the independent validation of the electromagnetic, mechanical and acoustic fields for uncoupled problems in Sections 5.1. Secondly, we include validation of coupled physics problems and application to challenging industrial benchmarks in Section 5.2.

In order to analyse the quality of the solutions, we set $\|e\|_{L^2} = (e,e)^{1/2}$, $\|e\|_{H^1} = (\|e\|_{L^2}^2 + \|\nabla e\|_{L^2}^2)^{1/2}$ for appropriate scalar and vectorial errors respectively, where $(e,e) = \int_\Omega e \cdot \overline{e} \, d\Omega$ is the standard L^2 inner product where the overbar denotes the complex conjugate. For mechanical problems, we also consider $\|\sigma(e)\|_{SNS(\Omega)} := \|\text{tr}(\sigma(e))\|_{L^2}$ associated with the sum of normal stresses to examine the extent to which our formulation can overcome mechanical locking [16].

5.1. Validation of single-physics problems

5.1.1. Conducting sphere in uniform alternating magnetic field. A closely related problem to the solution of (1), with $\boldsymbol{J}^s = \boldsymbol{J}^l = \boldsymbol{0}$, is that of a conducting object located in free space excited by a uniform harmonic background magnetic field of amplitude $\boldsymbol{H}_0$ and frequency ω. In this case, $\mu_0^{-1}\nabla \times \boldsymbol{A} \rightarrow \boldsymbol{H}_0$ as $|\boldsymbol{x}| \rightarrow \infty$. For a spherical conductor $\Omega_c = \{\boldsymbol{x} : |\boldsymbol{x}|^2 \leqslant R^2\}$ of radius R, permeability μ_s and conductivity γ_s, as illustrated in Figure 8, an analytical axisymmetric solution is presented in [43] for A_ϕ.

We consider the case of $R = 1$m, $\gamma_s = 10^7$S/m, $\mu_s = \mu_0$, $\boldsymbol{H}_0 = \mu_0^{-1}\boldsymbol{e}_z$Wb and angular frequencies $\omega = [5, 50, 500]$rad/s. To simulate this problem, the computational domain is chosen as $\Omega^m = ([0,4] \times [-4,4])$m^2 and we solve a suitably simplified version of Algorithm 1 where $\delta_{A_\phi hp}|_{\partial\Omega_n} = A_\phi|_{\partial\Omega_n}$ and we set $A_\phi^{hp} := \delta_{A_\phi hp}$. We generate a coarse mesh of 578 unstructured quasi-uniform triangular elements of maximum size $h = 0.5$m and use here, and subsequently, a blending function approach to represent the exact geometry of the sphere's surface [44]. This function avoids any geometrical error in the solution because of coarse approximation of the boundary. In light of the smooth nature of the solution, we consider uniform polynomial enrichment corresponding to $p = 1, 2 \ldots, 10$ on this mesh and plot in Figure 9 the relative error measures $\|A_\phi - A_\phi^{hp}\|_{L^2}/\|A_\phi\|_{L^2}$, $\|A_\phi - A_\phi^{hp}\|_{H^1}/\|A_\phi\|_{H^1}$ against the number of degrees of freedom for varying frequencies of the alternating magnetic field.

Figure 9a shows the convergence of the error against the number of degrees of freedom on a logarithmic scale, where each point represents a polynomial refinement and the different curves correspond to different frequencies and error measures. Each line indicates a downward sloping
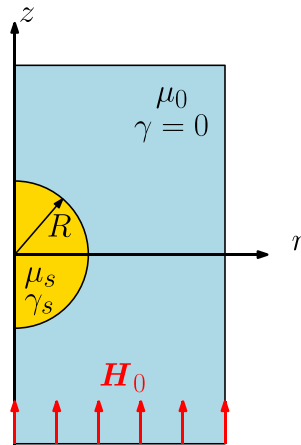

Figure 8. Conducting sphere in a uniform alternating magnetic field: problem setup.
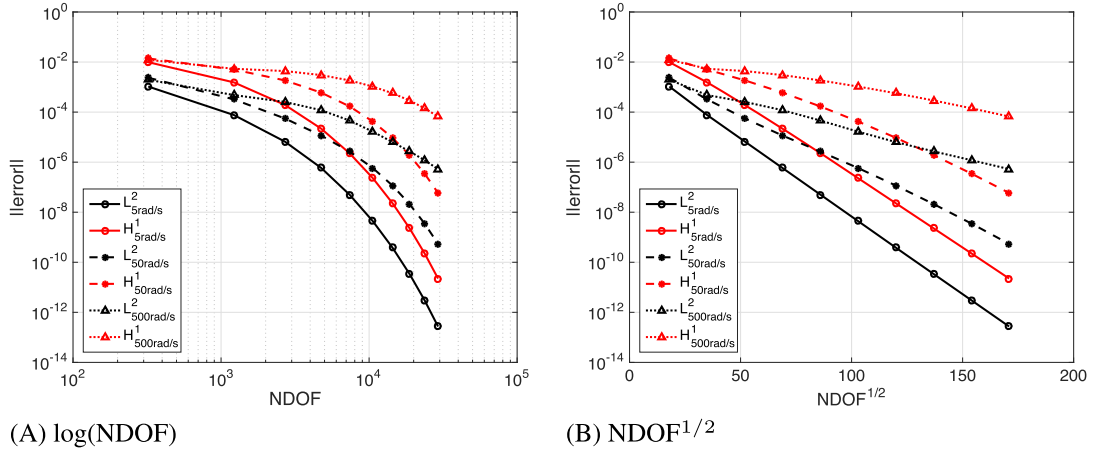
(A) log(NDOF) (B) NDOF$^{1/2}$

Figure 9. Conducting sphere in a uniform alternating magnetic field: convergence of $\|A_\phi - A_\phi^{hp}\|_{L^2}/\|A_\phi\|_{L^2}$ and $\|A_\phi - A_\phi^{hp}\|_{H^1}/\|A_\phi\|_{H^1}$ under p-refinement.
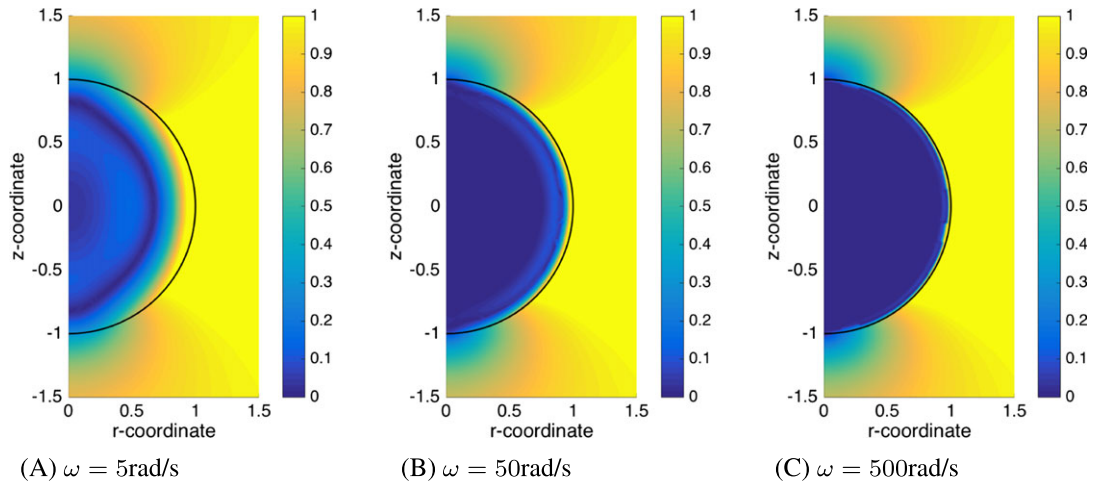

(A) $\omega = 5$rad/s (B) $\omega = 50$rad/s (C) $\omega = 500$rad/s

Figure 10. Conducting sphere in a uniform alternating magnetic field: contours of $|\boldsymbol{B}| \approx |\nabla \times (A_\phi^{hp} \boldsymbol{e}_\phi)|$ around the conducting sphere at different frequencies.

curve suggesting that the convergence is exponential. This is confirmed by plotting the error on a logarithmic scale against the number of degrees of freedom raised to the power $1/2$ on an algebraic scale in Figure 9b. After a pre-asymptotic region, each curve becomes a straight line indicating that convergence of the numerical to the analytical solution is exponential with respect to the square root number of degrees of freedom for p-refinement of this problem. This corresponds to the expected rate for smooth solutions, as reported by Babuška and Guo [45]$^{\|}$. As the frequency of the alternating magnetic field increases, the gradient of the lines in Figure 9b reduces, indicating that, although still exponential, the rate of convergence is lower. Physically, this is due to the smaller skin depths $s = \sqrt{2/(\omega\gamma\mu)}$, [43] which characterises the depth to which the eddy currents $\boldsymbol{J}^o = \gamma\boldsymbol{E} \approx \mathrm{i}\omega\gamma A_\phi^{hp} \boldsymbol{e}_\phi$ decay to $1/e$ of their surface value, associated with higher ω. It is possible to improve the gradient in the plots in Figure 9b by using a graded mesh towards the sphere's surface.

$^{\|}$We have also conducted h-refinement studies, which achieve the expected (and slower) algebraic rates of convergence for this problem. [45]

To illustrate the different fields and skin depth effects for different frequencies, Figure 10 shows the contours of $|\mathbf{B}| \approx |\nabla \times (A_\phi^{hp} \mathbf{e}_\phi)|$ for the various frequencies of the converged solutions. This figure illustrates the smaller s for higher ω and the need to use higher fidelity discretisations to capture the solution with the same degree of accuracy.

5.1.2. Mechanical shell. To verify the treatment of the elasticity system, we consider the solution of equation (2) for $\boldsymbol{\sigma}^e = \mathbf{0}$ and static displacements $\mathbf{u} \neq \mathbf{u}(t)$ for the case of a spherical mechanical shell $\Omega = \Omega_c = \{\mathbf{x} : r_i^2 \leqslant |\mathbf{x}|^2 \leqslant r_o^2\}$ of inner and outer radii r_i, r_o, respectively. The inner and outer surfaces of the shell are subject to traction conditions $-\hat{p}_i\mathbf{n}$ and $-\hat{p}_o\mathbf{n}$ resulting from internal and external pressures $\hat{p}_i$, $\hat{p}_o$ respectively, on different parts of $\partial\Omega^N$ as illustrated in Figure 11. This problem is axisymmetric and has the analytical solution [46], which can be expressed in terms of the cylindrical displacement components (u_r, u_z).

Specifically, we solve the problem corresponding to $r_i = 0.5$m, $r_o = 1$m, $E = 210 \times 10^9$Pa, $\nu = 0.49$, $\hat{p}_i = \hat{p}_o = 10^4$Pa so that the shell is nearly incompressible. As described in Section 2.2, we must fix part of the boundary of the shell to avoid it floating away. We solve a suitably simplified
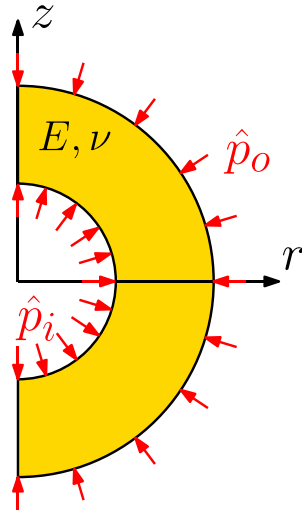

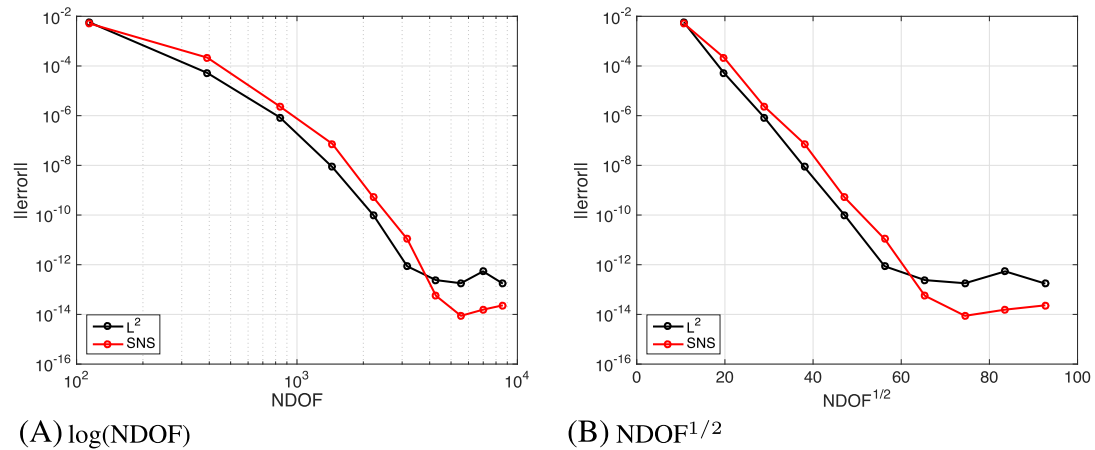Figure 11. Mechanical shell subject to interior and exterior pressure: problem setup.

(A) log(NDOF)

(B) NDOF$^{1/2}$

Figure 12. Mechanical shell subject to interior and exterior pressure: convergence of $\|\mathbf{u} - \mathbf{u}^{hp}\|_{L^2}/\|\mathbf{u}\|_{L^2}$, $\|\mathbf{u} - \mathbf{u}^{hp}\|_{SNS}/\|\mathbf{u}\|_{SNS}$ under p-refinement.

version of (20) for a single iteration where we choose to fix the displacements $\boldsymbol{\delta}_{\tilde{u}hp}^{DC[0]} = u_r\boldsymbol{e}_r + u_z\boldsymbol{e}_z$ on a small boundary segment $\partial\Omega^D$ according to the analytical solution. The region of computation corresponds to $\Omega^m = \Omega_c^m = \{(r, z) : r_i^2 \leqslant (r^2 + z^2) \leqslant r_o^2\}$, which we discretise by a quasi-uniform mesh of 68 unstructured triangular elements of maximum size $h = 0.5$m. We perform the same p-refinement study that was described in Section 5.1.1 and now measure convergence using $\|\boldsymbol{u} - \boldsymbol{u}^{hp}\|_{L^2}/\|\boldsymbol{u}\|_{L^2}$, $\|\boldsymbol{u} - \boldsymbol{u}^{hp}\|_{SNS}/\|\boldsymbol{u}\|_{SNS}$ where $\boldsymbol{u}^{hp} := \boldsymbol{\delta}_{\tilde{u}hp}$. The results shown in Figure 12a and 12b illustrate similar trends to those shown previously indicating that exponential convergence with respect to the number of degrees of freedom raised to the power $1/2$ is also achieved through p-refinement for the mechanical problem. In particular, p-refinement serves as a method for overcoming volumetric locking that is known to be associated with the displacement formulation of elasticity for nearly incompressible material [47,48] and leads to exponential rates of convergence of the error measured in the *SNS* norm. Although we do see stagnation of convergence when the norms of the error reach 10^{-13}, which coincides with the numerical precision of our computation. The displacements in the radial and axial directions of the shell, obtained using $p = 10$, are illustrated in Figure 13.

5.1.3. Acoustic scattering of a sphere. Finally, to verify the acoustic system (3, 4), we consider the problem of a sound hard sphere of radius R, illustrated in Figure 14. The sphere is illuminated by a harmonic incident wave $\hat{p}^{in} = \hat{p}_0 e^{\mathrm{i}kz}$ of amplitude $\hat{p}_0$ and wavenumber $k := \omega/c$. The complete solution is of the form $\hat{p} = \hat{p}^{in} + \hat{p}^{sc}$, subject to the boundary condition $\boldsymbol{n} \cdot \nabla\hat{p} = 0$ on $\partial\Omega_c$ and admits an axisymmetric analytical solution for $\hat{p}^{sc}$, [49]

Specifically, we choose to solve the problem corresponding to $R = 1$m, $\hat{p}_0 = 1$ Pa, $k = [4\pi/3, 10, 30]$m^{-1}. We solve a suitably simplified version of Algorithm 1 on the computational domain $\Omega^m = ([0, 5.6] \times [-5.6, 5.6])\backslash\{(r, z) : r^2 + z^2 \leqslant R^2\}$m^2 of which $\Omega_{pml}^m = \Omega^m\backslash([0, 4] \times [-4, 4])$m^2, with thickness parameters $[t_r, t_z] = [1.6, 1.6]$m, distance parameters $[d_r, d_z] = [4, 4]$m and $\delta_{\hat{p}hp} = 0$ on $\partial\Omega^m$. We fix a quasi-uniform mesh of 408 unstructured triangular elements of maximum size $h = 0.5$m and perform the same refinement study of $p = 1, 2 \ldots, 10$ as previously and measure convergence using $\|\hat{p}^{sc} - \hat{p}^{schp}\|_{L^2}/\|\hat{p}^{sc}\|_{L^2}$, $\|\hat{p}^{sc} - \hat{p}^{schp}\|_{H^1}/\|\hat{p}^{sc}\|_{H^1}$, where $\hat{p}^{schp} := \delta_{\hat{p}hp}$.

Figure 15a and 15b illustrates similar downward sloping trends, as shown in the previous examples. However, in this case the pre-asymptotic region is now affected by the increase in wave number. For higher wave numbers there is an initial stage of increase in error, which results from wave dispersion effects, discussed in [31] and [50]. This effect is overcome by further increasing p and eventually
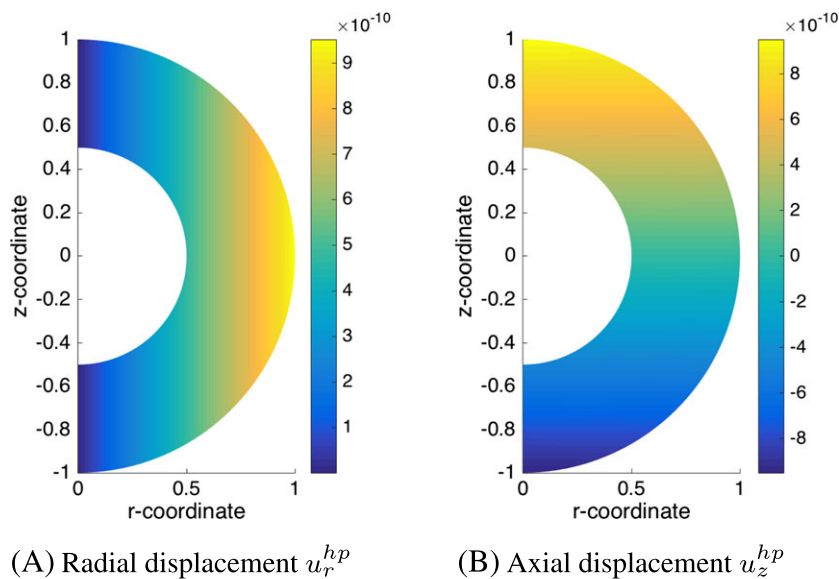

(A) Radial displacement u_r^{hp} (B) Axial displacement u_z^{hp}

Figure 13. Mechanical shell subject to interior and exterior pressure: contours of u_r^{hp} and u_z^{hp}.
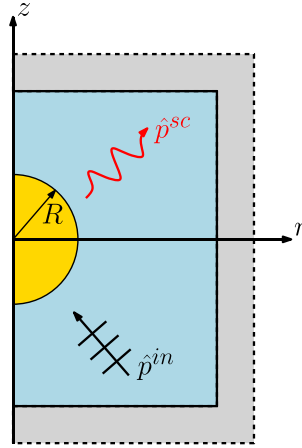
Figure 14. Sound-hard sphere subject to an incident acoustic pressure field: problem setup.
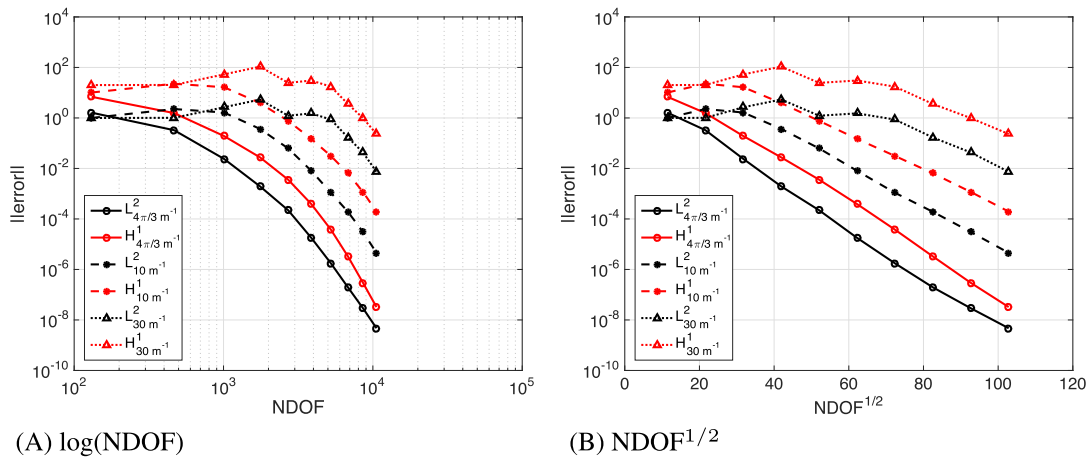

(A) log(NDOF) (B) NDOF$^{1/2}$

Figure 15. Sound-hard sphere subject to an incident acoustic pressure field: convergence of $\|\hat{p}^{sc} - \hat{p}^{schp}\|_{L^2}/\|\hat{p}^{sc}\|_{L^2}$, $\|\hat{p}^{sc} - \hat{p}^{schp}\|_{H^1}/\|\hat{p}^{sc}\|_{H^1}$ under p-refinement.

results in the same expected exponential rates of convergence as before, confirmed in Figure 15b. This again indicates that exponential convergence with respect to the number of degrees of freedom raised to the power $1/2$ is also achieved through p-refinement for the acoustic problem, provided sufficiently high refinement is used to eliminate numerical dispersion. For the case of $k = 4\pi/3$ m^{-1} for $p > 7$, the convergence behaviour is suboptimal because of the effect of the PML, which is an approximate absorbing boundary condition, but nevertheless, accurate solutions are still obtained. The finest solution, using $p = 10$, of the scattered pressure field arising from the incident pressure field for wave numbers $k = [4\pi/3, 10, 30]$ m^{-1} are illustrated in Figure 16.

5.2. Coupled multi-physics problems

5.2.1. Acoustic wave scattering of thin elastic shell. We consider a coupled acousto-mechanical problem consisting of a thin elastic shell of thickness t, mid surface radius R and material parameters ρ_s, ν and E. The shell is placed in a background medium described by ρ_f and c_f and is illuminated by harmonic incident pressure field $\hat{p}^{in}$. The configuration is illustrated in Figure 17. This problem requires the solution of Equation (7) in absence of electromagnetic coupling and naturally lends itself to a harmonic treatment. For thin shells, the solution to this problem can be approximated by
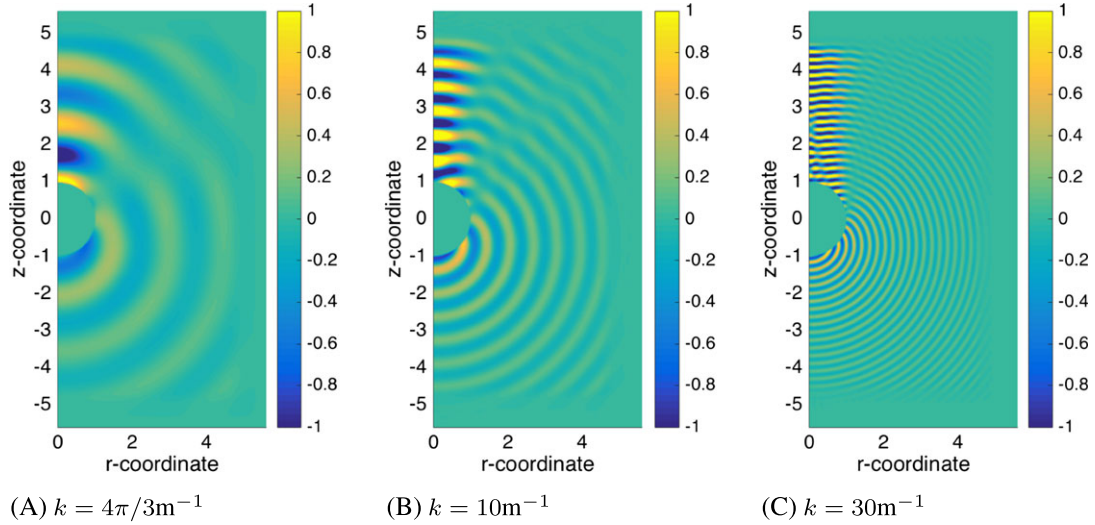
(A) $k = 4\pi/3 \mathrm{m}^{-1}$ (B) $k = 10 \mathrm{m}^{-1}$ (C) $k = 30 \mathrm{m}^{-1}$

Figure 16. Sound-hard sphere subject to an incident acoustic pressure field: contours of $\mathrm{Re}(\hat{p}^{sc\ hp})$.
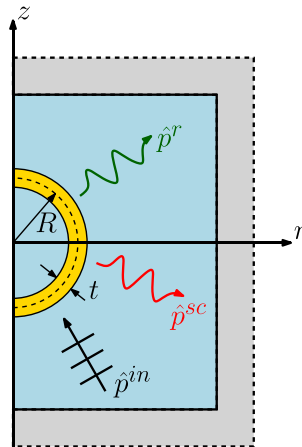

Figure 17. Elastic shell subject to an incident acoustic pressure field: problem setup.

the Kirchhoff shell theory [49,51] and the total pressure exterior becomes $\hat{p} = \hat{p}^{in} + \hat{p}^{sc} + \hat{p}^{r}$. For the incident field $\hat{p}^{in} = \hat{p}_0 e^{\mathrm{i}kz}$, the component $\hat{p}^{sc}$ corresponds to the hard scattering by the sphere and $\hat{p}^{r}$ to the radiated pressure [49,51].

We consider the particular case of $t = 0.05\mathrm{m}$, $R = 1\mathrm{m}$, $\hat{p}_0 = 1$ Pa, $k = \omega/c_f = [4\pi/3, 10, 30]$ m^{-1}, $\rho_f = 1000$ kg/m^3, $c_f = 1460$m/s, $\rho_s = 7800$ kg/m^3, $\nu = 0.3$, $E = 210$GPa. We treat this problem computationally by applying a suitably simplified version of Algorithm 1 with $\hat{p}^{schp} + \hat{p}^{rhp} := \delta_{\hat{p}hp}$ on the computational domain $\Omega^m = ([0, 5.6] \times [-5.6, 5.6]) \backslash \{(r, z) : r^2 + z^2 \leqslant (R - t/2)^2\}$m^2 with the same PML settings as in Section 5.1.3. As in Section 5.1.2, to avoid the shell from floating away, we fix a small boundary segment $\partial\Omega^D$ to have displacements $\boldsymbol{u} = \boldsymbol{0}$. The problem is driven by the incident pressure field in the form of a Neumann condition set on the external boundary of the shell $\{(r, z) : r^2 + z^2 = (R + t/2)^2\}$ as $\boldsymbol{n} \cdot \nabla\delta_{\hat{p}hp} = -\boldsymbol{n} \cdot \nabla\hat{p}^{in}$ and the coupling according to the interface conditions in equation (7). The inside boundary of the shell is left free and the acoustic effects inside of the shell are ignored.

Given that the convergence rates of the mechanical and acoustic fields have already been verified in Sections 5.1.2 and 5.1.3, we now instead directly compare the effectiveness of both h-refinement and

p-refinement with the analytical solution for $k = 4\pi/3\text{m}^{-1}$. In Figure 18, we plot various hp-enriched solutions for the line segment $1.025 \text{ m} \leqslant r \leqslant 5.6 \text{ m}$, $z = 0$, taken from the outer surface of the shell to the truncated boundary. For both h-refinement and p-refinement, the computed solution tends to the analytical for $r \leqslant 4$ m. However, for h-refinement, a mesh of $h \approx 0.1$m with 15 752 elements, with 7779 unknowns, is required to obtain good agreement with the analytical solution, with a level of accuracy of $O(10^{-2})$. On the other hand, using $p = 2$ on a mesh with 530 elements requires only 1021 unknowns for comparable accuracy in the solution. If we further refine p to $p = 4$, then the number of unknowns increases to 4163, but with improvement in the relative accuracy of two orders of magnitude. The PML is defined by the grey area, in which the computed solution is non-physical and absorbed.

Figure 19 shows the comparisons in computed and analytical solutions for higher wave numbers of $k = [10, 30]\text{m}^{-1}$. For both cases, the order of $p = 4$, used to obtain the finest solution in Figure 18, offers reasonable agreement with the analytical solution and is able to capture the higher frequencies of the waves. However, for increasing wave numbers, our computed solution requires even further p-refinement in order to accurately capture the solution in these regions because of the aforementioned dispersion effects. The solution case for $p = 4$ and a suitably refined solution of each case is plotted
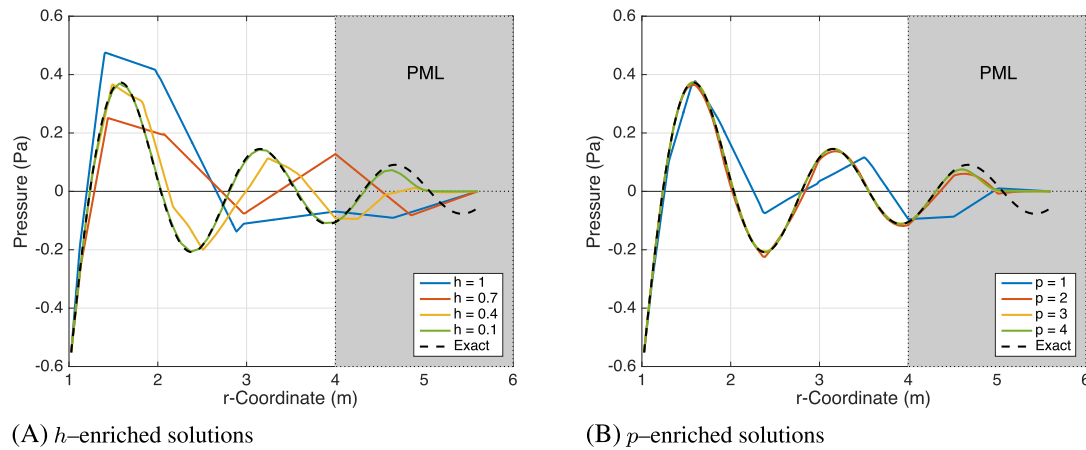

(A) h–enriched solutions

(B) p–enriched solutions

Figure 18. Elastic shell subject to an incident acoustic pressure field: Effects of h-refinement and p-refinement on the acoustic pressure field.
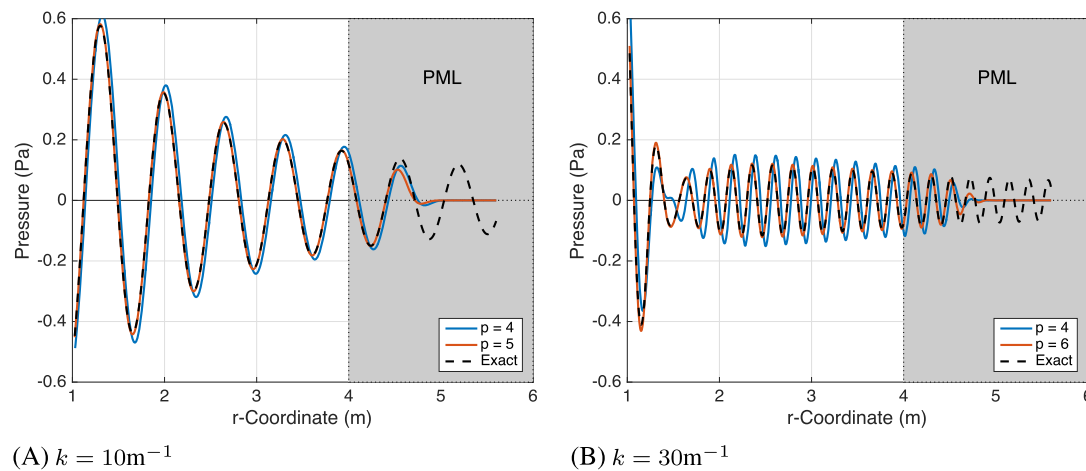

(A) $k = 10\text{m}^{-1}$

(B) $k = 30\text{m}^{-1}$

Figure 19. Elastic shell subject to an incident acoustic pressure field: effects of p-refinement for high wave number k on the acoustic pressure field.

against the analytical solution in Figure 19a and b. The mesh density required, for $p = 1$ elements, to capture the high-frequency wave effects at $k = 30\mathrm{m}^{-1}$ becomes impractical for such geometries.

The interaction between the pressure field and the displacements of the shell is illustrated in Figure 20, where the computed deformed shape of the shell is plotted in the surrounding acoustic field.

The success of high-order hp discretisations for the preceding case studies motivates our strategy for the following industrial example, which does not have an analytical solution.

5.2.2. Siemens benchmark problem. We now consider an industrially relevant benchmark problem, proposed by Siemens Magnet Technology, in which a simplified quarter-size representation of an MRI scanner was modelled and previously presented in [2]. The problem setup comprises of the same main components illustrated in Figure 1, with a reduced complexity in the coil configuration. The setup comprises of three metallic shields known as the outer vacuum chamber (OVC) Ω_c^{OVC}, $77°K$ radiation shield Ω_c^{77K} and $4°K$ helium vessel Ω_c^{4K}, which make up Ω_c and each with different material parameters (γ, μ, ν, E, ρ). A pair of main coils, with static current source $\boldsymbol{J}^{DC}$, are located on the outside of the three shields and a pair of gradient coils, with alternating current source $\boldsymbol{J}^{AC}(t)$, are located within the imaging bore. Both are assumed as Biot–Savart coils and are illustrated in Figure 21.

We treat this problem computationally for two cases; in the first case, we apply a suitably simplified version of Algorithm 1 in which we neglect the acoustic effects and focus on the purely magneto-mechanical coupling mechanisms, as in [2]. In the second case, we consider the fully coupled acousto-magneto-mechanical systems in Algorithm 1. We truncate the non-conducting
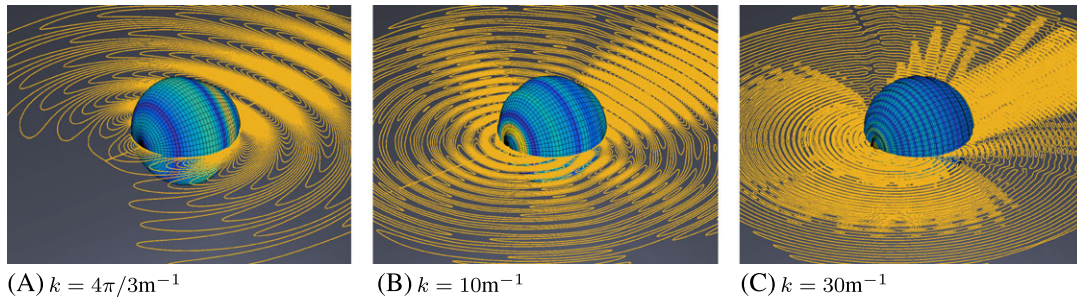

(A) $k = 4\pi/3\mathrm{m}^{-1}$ (B) $k = 10\mathrm{m}^{-1}$ (C) $k = 30\mathrm{m}^{-1}$

Figure 20. Elastic shell subject to an incident acoustic pressure field: deformed shell interacting with surrounding acoustic pressure field.

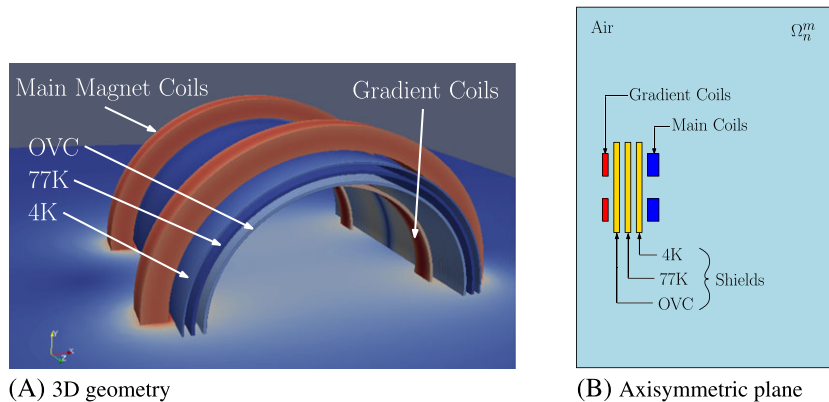(A) 3D geometry   (B) Axisymmetric plane

Figure 21. Simplified magnetic resonance imaging scanner subject to alternating and static current driven coils: problem setup.

region, comprised of air, and create the domain $\Omega^m = ([0, 1.26] \times [-1.68, 1.68])\text{m}^2$, with the PML $\Omega^m_{pml} = \Omega^m \backslash ([0, 0.9] \times [-1.2, 1.2])\text{m}^2$. As in Section 5.1.2, to avoid the shell from floating away, we fix a small boundary segment $\partial\Omega^D_c$ of the conductors to have displacements $\boldsymbol{u} = \boldsymbol{0}$. The exact geometries and material parameters of the conducting components are confidential and so are not to be displayed in this paper. We analyse the solution for an unstructured mesh of 8464 triangles of maximum size $h = 0.25\text{m}$, but with substantial refinement in Ω^m_c. Of these elements, ~ 1700 are located within Ω^m_c. This example serves to show the predictive capability of our approach, and to validate our approach, we compare our results with industrial data supplied by Siemens Magnet Technology.

Dissipated power and eddy currents A quantity of industrial interest is the power dissipated in Ω^{OVC}_c, Ω^{77K}_c and Ω^{4K}_c. This measure is used to quantify the resonance behaviour of the MRI system and to determine the frequencies at which operation is undesirable. This measure is given in terms of the Ohmic currents, and for the harmonic component of the magnetic vector potential $\delta_{A_{\phi hp}}$, becomes

$$P^o_\Omega(\omega, \boldsymbol{\delta}_A) = \frac{1}{2}\int_\Omega \gamma^{-1}|\boldsymbol{J}^o|^2 \mathrm{d}\Omega = \frac{1}{2}\int_\Omega \gamma|\boldsymbol{E}|^2\mathrm{d}\Omega \approx \pi\omega^2 \int_{\Omega_m}\gamma\left|\delta_{A_{\phi hp}}\right|^2 r\mathrm{d}\Omega^m. \tag{21}$$

In, [2] we previously compared $P^o_{\Omega^{OVC}_c}(\omega, \boldsymbol{A}_{AC})$, $P^o_{\Omega^{77K}_c}(\omega, \boldsymbol{A}_{AC})$ and $P^o_{\Omega^{4K}_c}(\omega, \boldsymbol{A}_{AC})$, where $\boldsymbol{A}_{AC} \approx A^{hp}_\phi \boldsymbol{e}_\phi$ is the equivalent to $\delta_{A_{\phi hp}}\boldsymbol{e}_\varphi$ but obtained by the fixed point scheme, to a set of industrial results using the NACS software [11]. We revisit this by including the results of the new monolithic formulation, both with and without acoustic effects. The converged results are plotted in Figure 22 where we

(A) $P^o_{\Omega^{OVC}_c}(\omega, \boldsymbol{A}_{AC})$

(B) $P^o_{\Omega^{77K}_c}(\omega, \boldsymbol{A}_{AC})$

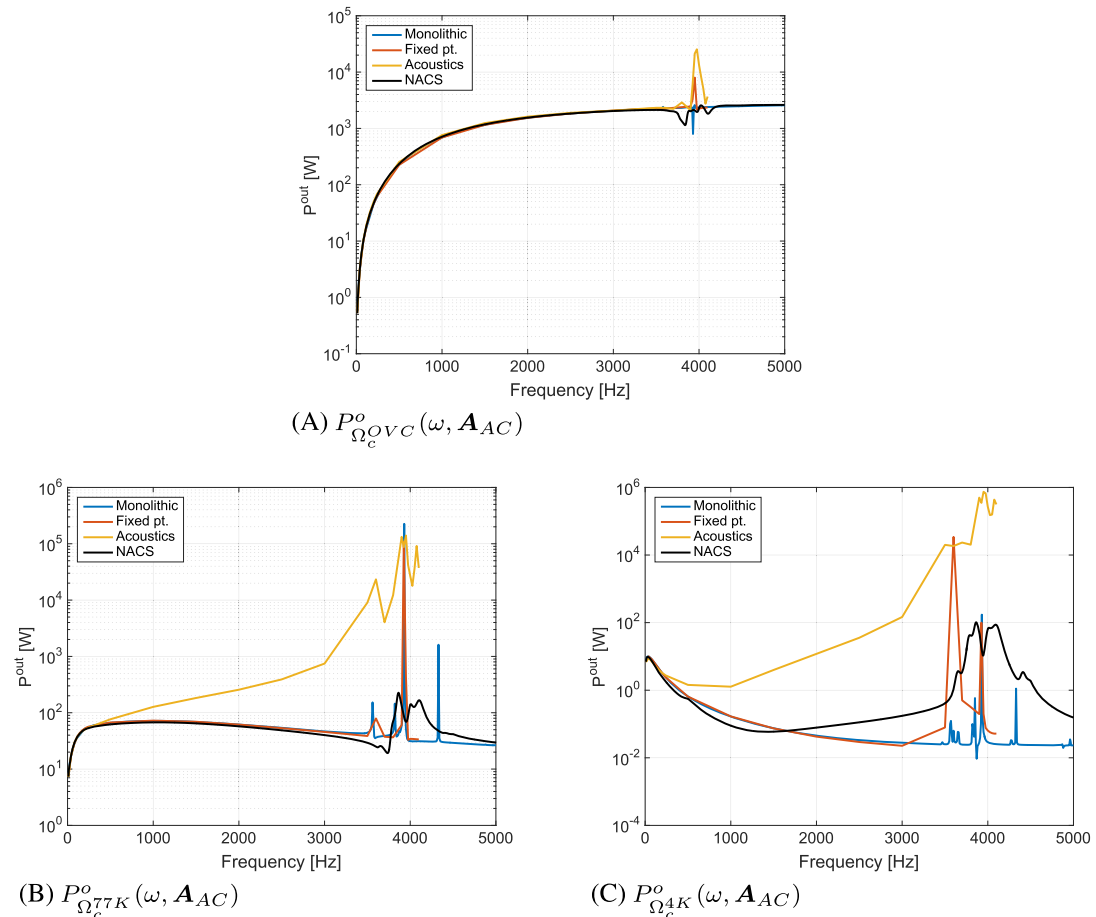(C) $P^o_{\Omega^{4K}_c}(\omega, \boldsymbol{A}_{AC})$

Figure 22. Simplified magnetic resonance imaging scanner subject to alternating and static current driven coils: Ohmic power dissipation as a function of alternating current frequency

(A) $f = 160\text{Hz}, p = 1$ (B) $f = 160\text{Hz}, p = 5$ (C) $f = 4100\text{Hz}, p = 1$ (D) $f = 4100\text{Hz}, p = 5$
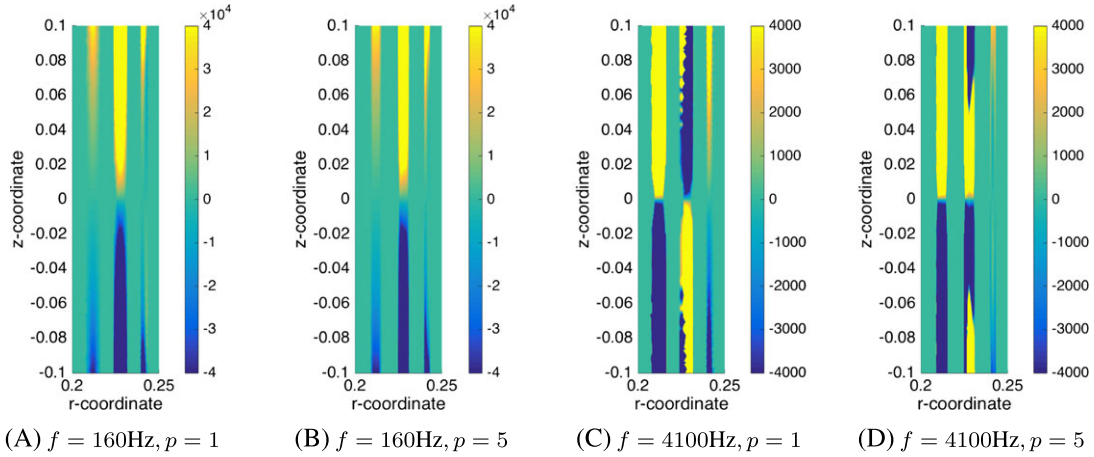
Figure 23. Simplified magnetic resonance imaging scanner subject to alternating and static current driven coils: contours of the eddy currents $\text{Re}(J_\phi^o)$ for $p = 1, 5$ and $f = [160, 4100]$Hz.
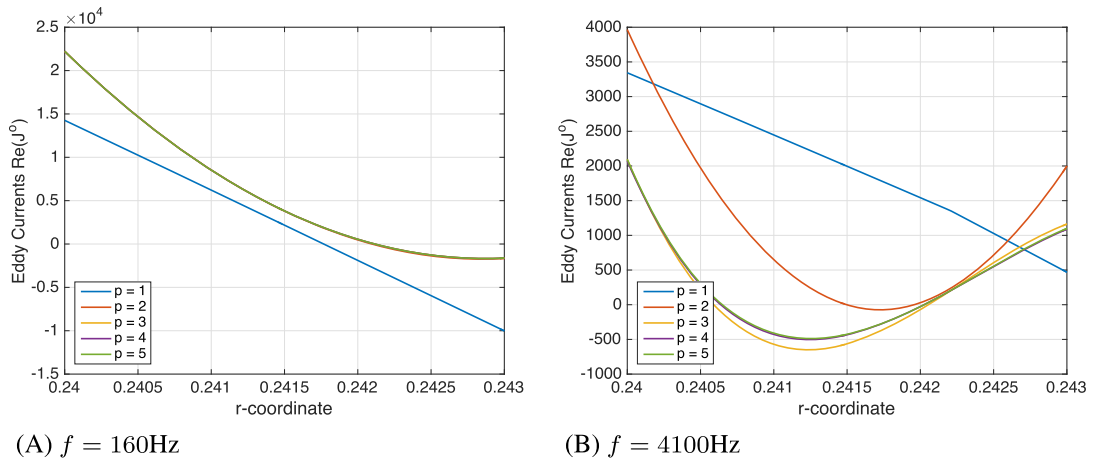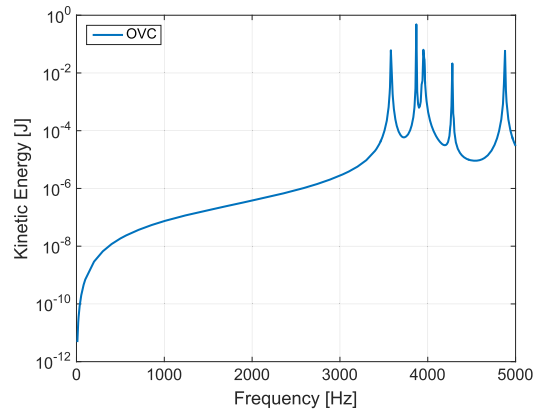

(A) $f = 160\text{Hz}$ (B) $f = 4100\text{Hz}$

Figure 24. Simplified magnetic resonance imaging scanner subject to alternating and static current driven coils: effects of p-enrichment on the eddy current resolution $\text{Re}(J_\phi^o)$ in Ω_c^{4K} for $f = [160, 4100]$Hz.

perform a sweep over the alternating current driving frequencies in the range $\omega := 2\pi f = 2\pi(10 \leqslant f \leqslant 5000)$ rad/s. In the figure, the black line represents the results obtained by Siemens using NACS, the red line the results of the previous fixed point scheme, the blue line our new monolithic magneto-mechanical formulation and the yellow line the fully coupled monolithic system with acoustic effects.

In the absence of acoustic effects, and for $f \leqslant 3000$ Hz, the fixed point, monolithic and NACS results for $P_{\Omega_c^{OVC}}^o(\omega, A_{AC})$ and $P_{\Omega_c^{77K}}^o(\omega, A_{AC})$ are in close agreement with each other because in this case the problem is well approximated by the pure eddy current model. The fixed point and monolithic results for $P_{\Omega_c^{4K}}^o(\omega, A_{AC})$ also give good agreement in this region; however, the results obtained by NACS offer very small differences of $O(10^{-1})$ for $f > 1000$Hz. We conjecture that this is due to the limitations of the low-order elements in accurately resolving the skin depth effects with increasing frequency, illustrated in Figures 23 and 24. These methodologies also give a similar prediction of the resonance region occupied by 3500 Hz $\leqslant f \leqslant$ 4500 Hz with the NACS model being damped because of the artificial Rayleigh damping [52]. The effect of this damping on the response of the system results in a change in the amplitude and frequency range of the resonance region [52,53].

Our new monolithic framework offers computational advantages over our previous fixed point strategy because the solution is obtained in a single iteration, as opposed to multiple iterations, which grows in the resonance region. This enables us to perform rapid and robust solutions at each frequency, which offers trivial parallelism and greater resolution in the resonance region for the same computational cost. Notably, the resonant frequencies computed using the fixed point scheme exactly match those obtained by the monolithic scheme albeit with differing magnitude of the peaks because of the effects of matrix equation conditioning.

The predicative capability of our approach is further demonstrated by the inclusion of acoustic effects, which has substantial effects in $P^o_{\Omega^{77K}_c}(\omega, A_{AC})$ and $P^o_{\Omega^{4K}_c}(\omega, A_{AC})$ for $f \geq 500$ Hz, not included in the NACS software or our previous fixed point scheme. Negligible effects for $P^o_{\Omega^{ovc}_c}(\omega, A_{AC})$ are obtained because the OVC is located closest to the inner bore tube and, therefore, the gradient coils, and dissipated power is dominated by the electromagnetic effects. In contrast, the other two shields are located to the outside of the OVC and hence acoustic propagation effects cause these shields to further perturb the output power. Note that repeating the results with coils treated as deformable conductors leads to only negligible changes in the output power, and therefore, these results are not shown.
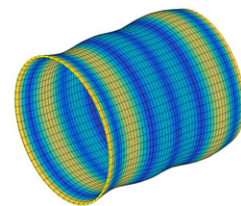

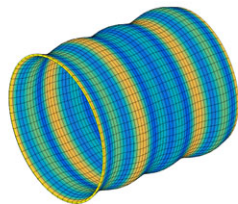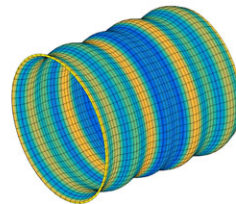(A) $T_{\Omega^{OVC}_c}(\omega, \delta_u))$
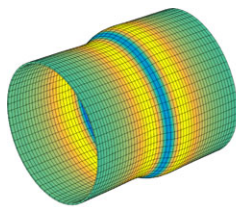
(B) 3580 Hz
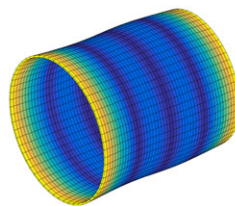
(C) 3870 Hz

(D) 3950 Hz

(E) 4280 Hz

(F) 4880 Hz

Figure 25. Simplified magnetic resonance imaging scanner subject to alternating and static current driven coils: $T_{\Omega^{ovc}_c}(\omega, \delta_u)$ and resonant mode shapes.

To illustrate the different skin effects at different frequencies, we show in Figure 23 the eddy current distributions at $f = 160$Hz and $f = 4100$Hz for both $p = 1$ and $p = 5$. At the lower frequency, the skin effects are already well resolved by $p = 1$ elements, but the higher frequency $p \geqslant 4$ elements are required to resolve the small skin depth. This is further illustrated in Figure 24, which shows the convergence of J^o in Ω_c^{4K} along the line $z = 0.04$m for $p = 1, 2, \ldots, 5$.

5.2.2.1. Kinetic energy and mode shapes. The kinetic energy of Ω_c^{OVC}, Ω_c^{77K} and Ω_c^{4K} is of industrial interest for understanding the motion of the conductors, highlighting the resonance frequencies and the corresponding mode shapes of the scanner's structure. In terms of the computed displacements $\delta_{\tilde{u}\ hp}$, this is

$$T_\Omega(\omega, \delta_u) = \frac{1}{4}\int_\Omega m|v|^2 \mathrm{d}\Omega = \frac{1}{4}\int_\Omega \rho\omega^2|\delta_u|^2\mathrm{d}\Omega \approx \frac{\pi}{2}\int_{\Omega^m}\rho\omega^2|\delta_{\tilde{u}hp}|^2 r\mathrm{d}\Omega^m. \tag{22}$$

(A) 10 Hz (B) 1500 Hz
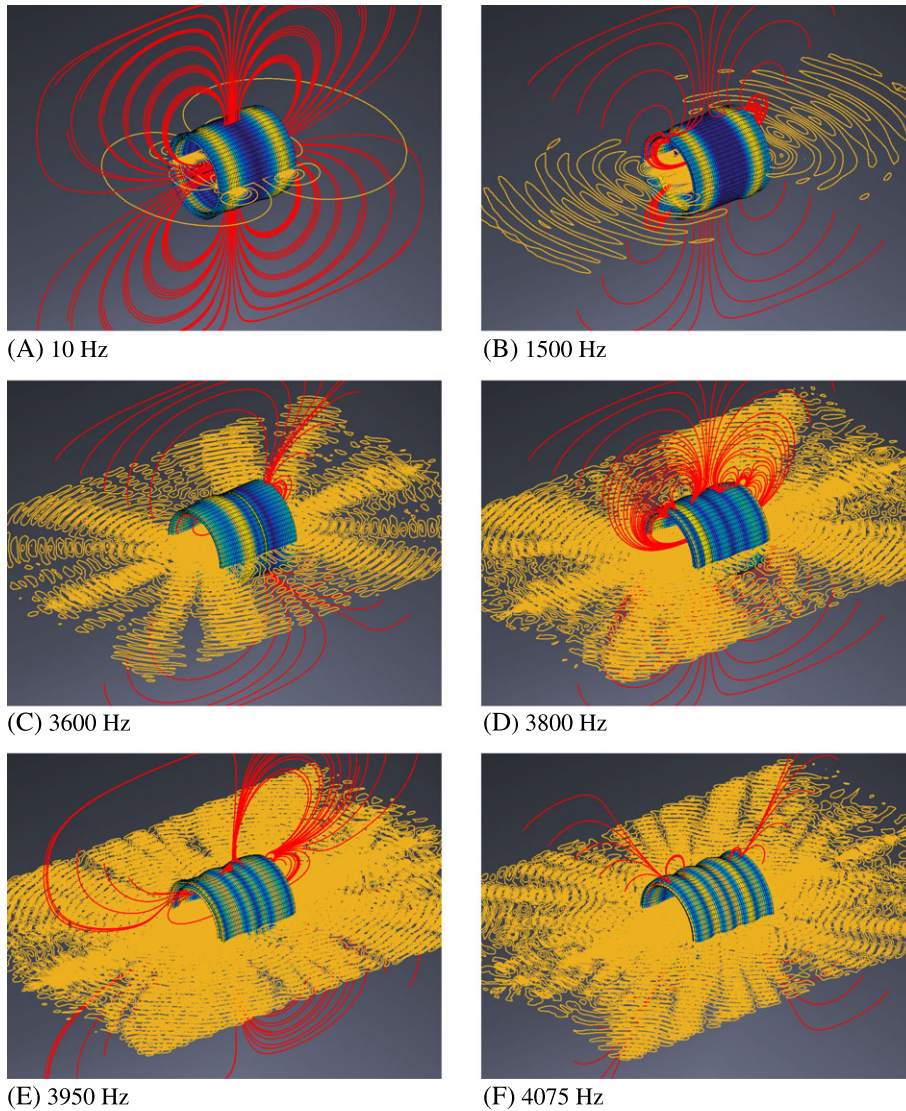
(C) 3600 Hz (D) 3800 Hz

(E) 3950 Hz (F) 4075 Hz

Figure 26. Simplified magnetic resonance imaging scanner subject to alternating and static current driven coils: magnetic flux lines (red), acoustic contour lines (yellow) and displaced shields Ω_c.

Figure 25 illustrates the kinetic energy as a function of the driving current frequency in the gradient coils in Ω_c^{OVC}. Similar mode shapes are also obtained for the other shields [54]. For each spike in the kinetic energy, or resonant frequency, a corresponding three-dimensional axisymmetric mode shape of the shield is included. Higher resonant frequencies excite higher order sinusoidal modes as the figures illustrate. The resonant frequencies of the kinetic energy in the shields coincide with the frequencies experienced in the output power, which suggests that the primary source of excitation in the conductors is that of the eddy currents dissipated in the shields.

Finally, we illustrate the complex behaviour of the magnetic flux lines, acoustic contour lines and deformed structure in Figure 26 for a range of frequencies in both the eddy current dominant (low frequency) and the resonance (high frequency) regions. This figure illustrates that in the low-frequency region ($120\text{Hz} \leqslant f \leqslant 1500\text{Hz}$), a patient in the bore can become exposed to sufficiently higher noise levels than that of the exterior region of the scanner, with the sound radiating and decaying outwards in space. This is due to the dominance of the harmonic magnetic field arising from the gradient coils, located inside the imaging volume, which gives rise to the source term in the acoustic Helmholtz system in (3). As the frequency increases ($1500\text{Hz} \leqslant f \leqslant 3700\text{Hz}$), the effect of the mechanical resonance begins to dominate and the acoustic field is further excited by the displacement of the shields and the sound intensity outside of the scanner increases. The case of $f = 4075\text{Hz}$ illustrates a higher frequency mode shape and the effect of the displacement on the acoustic field. In this case, the magnetic field is further perturbed because of the increase in Lorentz currents resulting from the acoustic excitation. Notably, in each case, the greatest sound intensity is that inside the bore tube, suggesting that the highest noise levels are experienced by the patient.

6. CONCLUSION

In this paper, we have provided a new rigorous theoretical framework for the simulation of acousto-magneto-mechanical effects in MRI scanners, which provide the basis of our design tool. We have provided a consistent linearisation of the transient equations and have arrived at a simplified monolithic single-step strategy in the case of harmonic gradient coil excitations. This greatly improves our previous work, [2] which required non-physically motivated simplifying assumptions and resulted in a fixed point strategy with a growth of iterations for increasing frequency. We have further extended our approach to include acoustic effects and discretised the resulting framework by hp-FEM to ensure a robust tool that provides the accurate resolution of small skin depths and wave propagation effects. The optimal convergence of the physical fields is demonstrated for a series of challenging single and multi-physics test cases in axisymmetric coordinates. The predictive capability has been illustrated by applying our approach to rapid evaluation of the performance of a MRI scanner model whose acousto-magneto-mechanical response has been analysed in detail. The next steps of our research involves developing a full three-dimensional simulation tool for MRI scanners based on hp-FEM.

REFERENCES

1. Grainger D. Safety Guidelines for Magnetic Resonance Imaging Equipment in Clinical Use. Medicines and Healthcare Products Regulatory Agency. http://webarchive.nationalarchives.gov.uk/20141205150130/http://www.mhra.gov.uk/home/groups/dts-iac/documents/publication/con2033065.pdf; 2015.
2. Ledger PD, Gil AJ, Poya R, Kruip M, Wilkinson I, Bagwell S. Solution of an industrially relevant coupled magneto-mechanical problem set on an axisymmetric domain. *Applied Mathematical Modelling*. 2016;**40**:1959-1971.

3. Schaefer D, Bourland J, Nyenhuis J. Review of patient safety in time-varying gradient fields. *Journal of Magnetic Resonance Imaging*. 2000;**12**:20-29.

4. Radomskij P, Schmidt MA, Heron CW, Prasher D. Effect of MRI noise on cochlear function. *The Lancet*. 2002;**359**:1485-1486.

5. Mollasadeghi A, Mehrparvar A, Atighechi S, Davari M, Shokouh P, Mostaghaci M, Bahaloo M. Sensorineural hearing loss after magnetic resonance imaging. *Case Reports in Radiology*. 2013;**2013**:3.

6. Cho ZH, Park SH, Kim lH, Chung SC, Chung ST, Chung IY, Moon CW, Yi IH, Sin CH, Wong EK. Analysis of acoustic noise in MRI. *Magnetic Resonance Imaging*. 1997;**15**:815-822.

7. Price DL, De Wilde JP, Papadaki AM, Curran JS, Kitney RI. Investigation of acoustic noise on 15 MRI scanners from 0.2 T to 3 T. *Magnetic Resonance Imaging*. 2001;**13**(2):288-93.

8. McJury M, Shellock F. Auditory noise associated with MR procedures: a review. *Magnetic Resonance Imaging*. 2000;**12**:37-45.

9. COMSOL Multiphysics Software. Available from: https://www.comsol.com. Accessed on 25th July 2016.

10. Ansys Software. Available from: http://www.ansys.com. Accessed on 25th July 2016.

11. NACS Finite Element Analysis Software. Available from: http://www.simetris.de/en/Table/Products/NACS-Finite-Element-Simulation/. Accessed on 25th July 2016.

12. Kaltenbacher M, Landes H, Lerch R. Software package for the numerical simulation of coupled field problems. *Transactions on Engineering Sciences*. 1999;**22**:233-242.

13. Rausch M, Gebhardt M, Kaltenbacher M, Landes H. Magnetomechanical field computations of a clinical magnetic resonance imaging (MRI) scanner. *The International Journal for Computation and Mathematics in Electrical and Electronic Engineering (COMPEL)*. 2003;**22**:576-588.

14. Rausch M, Gebhardt M, Kaltenbacher M, Landes H. Computer-aided design of clinical magnetic resonance imaging scanners by coupled magnetomechanical-acoustic modeling. *IEEE Transactions on Magnetics*. 2005;**41**:72-81.

15. Kaltenbacher M. *Numerical Simulation of Mechatronic Sensors and Actuators*. Berlin Heidelberg: Springer; 2004.

16. Gil AJ, Ledger PD. A coupled *hp*-finite element scheme for the solution of two-dimensional electrostrictive materials. *International Journal for Numerical Methods in Engineering*. 2012;**91**:1158-1183.

17. Jin D, Ledger PD, Gil AJ. An *hp*-fem framework for the simulation of electrostrictive and magnetostrictive materials. *Computers and Structures*. 2014;**133**:131-148.

18. Jin D, Ledger PD, Gil AJ. *hp*-Finite element solution of coupled stationary magnetohydrodynamics problems including magnetostrictive effects. *Computers and Structures*. 2016;**164**:161-180.

19. Guan M, Wang X, Ma L, h Zhou Y, Xin C. Magneto-mechanical coupling analysis of a superconducting solenoid magnet in self-magnetic field. *IEEE Transactions on Applied Superconductivity*. 2014;**24**(3):1-4.

20. Sánchez CC, Power H, Garcia SG, Bretones AR. Quasi-static multi-domain inverse boundary element method for MRI coil design with minimum induced E-field. *Engineering Analysis with Boundary Elements*. 2011;**35**(3):264-272.

21. Markiewicz DW, Vaghar MR, Dixon IR, Garmestani H. Generalized plane strain analysis of superconducting solenoids. *Journal of Applied Physics*. 1999;**86**(12):7039-7051.

22. Crozier SC, Liu F. Numerical evaluation of the fields induced by body motion in or near high-field MRI scanners. *Progress in Biophysics and Molecular Biology*. 2005;**87**(2-3):267-278.

23. Kaltenbacher M, Landes H, Lerch R. An efficient calculation scheme for the numerical simulation of coupled magnetomechanical systems. *IEEE Transactions on Magnetics*. 1997;**33**(2):1646-1649.

24. Kurz S, Fetzer J, Lehner G, Rucker WM. A novel formulation for 3D eddy current problems with moving bodies using a Lagrangian description and BEM-FEM coupling. *IEEE Transactions on Magnetics*. 1998;**34**(5):3068-3073.

25. Bouillaulta F, Buffab A, Madayc Y, Rapetti F. Simulation of a magneto-mechanical damping machine: Analysis, discretization, results. *Computer Methods in Applied Mechanics and Engineering*. 2002;**191**:2587-2610.

26. Kirschneck M, Rixen D, Polinder H, van Ostayen R. Effects of magneto-mechanical coupling on structural modal parameters. In: Topics in Modal Analysis II: Proceedings of the 32nd IMAC, A Conference and Exposition on Structural Dynamics, vol. 8, Brescia, Italy; 2014:11–18.

27. Hauck A, Lahmer T, Kaltenbacher M. Enhanced homogenization technique for magnetomechanical systems using the generalized finite element method. *The International Journal for Computation and Mathematics in Electrical and Electronic Engineering (COMPEL)*. 2009;**28**(4):935-947.

28. Ren Z, Razek A. A strong coupled model for analysing dynamic behaviours of non-linear electromechanical systems. *IEEE Transactions on Magnetics*. 1994;**30**(5):3252-3255.

29. Thompson LL. A review of finite-element methods for time-harmonic acoustics. *The Journal of the Acoustical Society of America*. 2006;**119**(3):1315-1330.

30. Ledger PD, Zaglmayr S. *hp*-Finite element simulation of three-dimensional eddy current problems on multiply connected domains. *Computer Methods in Applied Mechanics and Engineering*. 2010;**199**:3386-3401.

31. Ainsworth M. Discrete dispersion relation for *hp*-version finite element approximation at high wave number. *SIAM Journal on Numerical Analysis*. 2004;**42**:553-575.

32. Michler C, Demkowicz L, Kurtz J, Pardo D. Improving the performance of perfectly matched layers by means of hp-adaptivity. *Numerical Methods for Partial Differential Equations*. 2007;**23**:832-858.

33. Ammari H, Buffa A, Nedéléc JC. A justification of eddy currents model for the Maxwell equations. *SIAM Journal on Applied Mathematics*. 2000;**60**:1805-1823.

34. Monk P. *Finite Element Methods for Maxwell's Equations*. Oxford University Press: Oxford; 2003.

35. Gil AJ, Bonet J. Finite element analysis of prestressed structural membranes. *Finite Elements in Analysis and Design*. 2006;**42**(8-9):683-697.

36. Gil AJ. Structural analysis of prestressed saint venant-kirchhoff hyperelastic membranes subjected to moderate strains. *Computers and Structures*. 2006;**84**(15-16):1012-1028.
37. Gil AJ, Bonet J. Finite element analysis of partly wrinkled reinforced prestressed membranes. *Computational Mechanics*. 2007;**40**(3):595-615.
38. Poya R, Sevilla R, Gil AJ. A unified approach for a posteriori high-order curved mesh generation using solid mechanics. *Computational Mechanics*. 2016;**58**(3):457–490. DOI: 10.1007/s00466-016-1302-2.
39. Baek S, Gleason RL, Rajagopal KR, Humphrey JD. Theory of small on large: Potential utility in computations of fluid-solid interactions in arteries. *Computer Methods in Applied Mechanics and Engineering*. 2007;**196**:3070-3078.
40. Lacoste P. Solution of Maxwell equation in axisymmetric geometry by Fourier series decomposition and by use of $H(rot)$ conforming finite element. *Numerische Mathematik*. 2000;**84**(4):577-609.
41. Schöberl J, Zaglmayr S. High order Nédélec elements with local complete sequence properties. *The International Journal for Computation and Mathematics in Electrical and Electronic Engineering (COMPEL)*. 2005;**24**:374-384.
42. Zaglmayr S. High order finite element methods for electromagnetic field computation. *PhD Thesis*: Institut für Numerische Mathematik, Johannes Kepler Univerität Linz, Austria; 2006.
43. Smythe W. *Static and Dynamic Electricity*. USA: McGraw-Hill; 1950.
44. Szabó B, Babuška I. *Finite Element Analysis*. New York: John Wiley and Sons; 1991.
45. Babuška I, Guo BQ. The H, P and $H−p$ version of the finite element method: Basis theory and applications. *Advances in Engineering Software*. 1992;**15**:159-174.
46. Bower A. *Applied Mechanics of Solids*. Florida: CRC Press; 2009.
47. Suri M. Analytical and computational assessment of locking in the hp finite element method. *Computer Methods in Applied Mechanics and Engineering*. 1996;**133**:347-371.
48. Chilton L, Suri M. On the selection of a locking-free hp element for elasticity problems. *International Journal for Numerical Methods in Engineering*. 1997;**40**:2045-2062.
49. Chang YC, Demkowicz L. Scattering on a spherical shell. comparison of 3-D elasticity and Kirchhoff shell theory results. *Computer Assisted Mechanics and Engineering Sciences*. 1995;**2**:207-229.
50. Ihlenburg F. *Finite Element Analysis of Acoustic Scattering*: Springer Publishing Company, Incorporated: New York City; 1998.
51. Partridge C. Sound wave scattering from an elastic spherical shell. *Technical Report*; 1993. http://www.dtic.mil/dtic/tr/fulltext/u2/a264039.pdf.
52. Hughes TJR. *The Finite Element Method: Linear Static and Dynamic Finite Element Analysis*. Englewood Cliffs: Prentice-Hall; 1987.
53. Nashif AD, Jones DIG, Henderson JP. *Vibration Damping*. John Wiley & Sons: New Jersey; 1985.
54. Bagwell S. Title to be confirmed. *PhD Thesis*. Swansea University. In Preparation.